Fundamentals of metasurface lasers based on resonant dark states

Sotiris Droulias,[1,*] Aditya Jain,[2] Thomas Koschny,[2] and Costas M. Soukoulis[1,2]
[1]*Institute of Electronic Structure and Laser, FORTH, 71110 Heraklion, Crete, Greece*
[2]*Ames Laboratory and Department of Physics and Astronomy, Iowa State University, Ames, Iowa 50011, USA*
(Received 1 August 2017; revised manuscript received 8 October 2017; published 30 October 2017)

Recently, our group proposed a metamaterial laser design based on explicitly coupled dark resonant states in low-loss dielectrics, which conceptually separates the gain-coupled resonant photonic state responsible for macroscopic stimulated emission from the coupling to specific free-space propagating modes, allowing independent adjustment of the lasing state and its coherent radiation output. Due to this functionality, it is now possible to make lasers that can overcome the trade-off between system dimensions and Q factor, especially for surface emitting lasers with deeply subwavelength thickness. Here, we give a detailed discussion of the key functionality and benefits of this design, such as radiation damping tunability, directionality, subwavelength integration, and simple layer-by-layer fabrication. We examine in detail the fundamental design tradeoffs that establish the principle of operation and must be taken into account and give guidance for realistic implementations.

DOI: 10.1103/PhysRevB.96.155143

I. INTRODUCTION

In search of coherent light sources that can be integrated in small-scale photonic systems, nanolasers have been the object of sustained research in latest years [1–18]. In order to scale the laser dimensions down, many diverse materials and techniques have been utilized so far.

All-dielectric systems, such as vertical-cavity surface-emitting lasers [1], photonic crystal lasers [2,3], Fabry-Perot lasers [4], microdisk lasers [5], and ring-resonator based systems [6], may achieve extremely high Q factors ($\sim 10^3 - 10^6$), due to their very low material losses. These systems can offer significantly low lasing thresholds, but their size is limited to the order of magnitude of the operating wavelength, by principle of operation. On the other hand, one can actually reduce the laser size even to subwavelength scales with the aid of surface plasmon-polariton modes [7–17]. Typical configurations such as the spaser [7], the lasing spaser [8], and the plasmonic waveguide laser [9] have very recently demonstrated this concept. The necessary presence of metal, nevertheless, imposes large material losses and pushes the lasing threshold to high levels accordingly. More importantly, in all aforementioned implementations, the radiation damping is closely connected with the type of the oscillating mode. For example, nanospheres that typically operate with the lowest order electric mode (electric dipole Mie mode) in plasmonic nanolasers are affected not only by large dissipative losses, but by dipole radiation damping as well. Making the particle smaller, does help to reduce its radiation moment, but at the same time its stored energy becomes smaller and, hence, the part of the Q factor that is related to radiation loss does not improve. Making it bigger, allows operation with higher order modes of weaker radiating moments, given that the materials allow being still in the subwavelength regime. Hence, if one desires to change the radiation damping at the given operating frequency, then the system must be redesigned to operate—if possible—with a different mode.

In Ref. [18], we proposed a metamaterial laser system that resolves this predicament, by offering separate control of the energy storage and radiation mechanisms. The principle of operation is based on the excitation of a dark mode [19], i.e., a mode of zero net electric/magnetic moment that does not consequently radiate. Ideally, in the total absence of any material loss, if energy is transferred into the system it will be stored in the dark mode and will stay there indefinitely. With the aid of a small nonresonant scatterer, though, the dark mode can be coupled to radiation modes at will and the coupling can be simply controlled by the position, size and material of the scatterer. In essence, the Q factor of the system is controlled at will and, most importantly, independently of the resonance mechanism, which is responsible for the energy storage. The resonator is implemented as a thin slab, essentially a metasurface [20], which is chosen to be dielectric, in order to minimize the dissipative losses [21,22]. However, there is a distinction between typical active metasurfaces and our system. In the former systems the metamaterial resonators are directly coupled to gain and the whole system becomes an active metasurface [14,15,23–27]. In our case, *an explicit dark resonant mode with gain is outcoupled by an additional passive metasurface* and, therefore, the term "metasurface" refers to the outcoupling implementation alone, although the whole configuration can be considered as one composite metasurface.

The aim of this paper is to examine the fundamental properties and trade-offs that establish the principle of operation and that must be taken into account in realistic designs. In Sec. II, we repeat in brief the principle of operation and the basic properties of the laser for completeness. In Sec. III, we examine the effect of the two loss channels, namely the dissipative losses due to material absorption and the radiation damping due to coupling of the oscillating mode to radiating waves. In Sec. IV, we estimate the lasing threshold in terms of realistic material gain. In Sec. V, we examine the pumping efficiency of the gain material, when embedded in the structure. In Sec. VI, we discuss the limits and tunability of directional emission. Finally, in Sec. VII, we demonstrate alternative realizations that are more convenient to be implemented experimentally.

II. PRINCIPLE OF OPERATION

Our design laser consists of three basic parts: the gain material, the dark mode which serves as the resonator and

*sdroulias@iesl.forth.gr

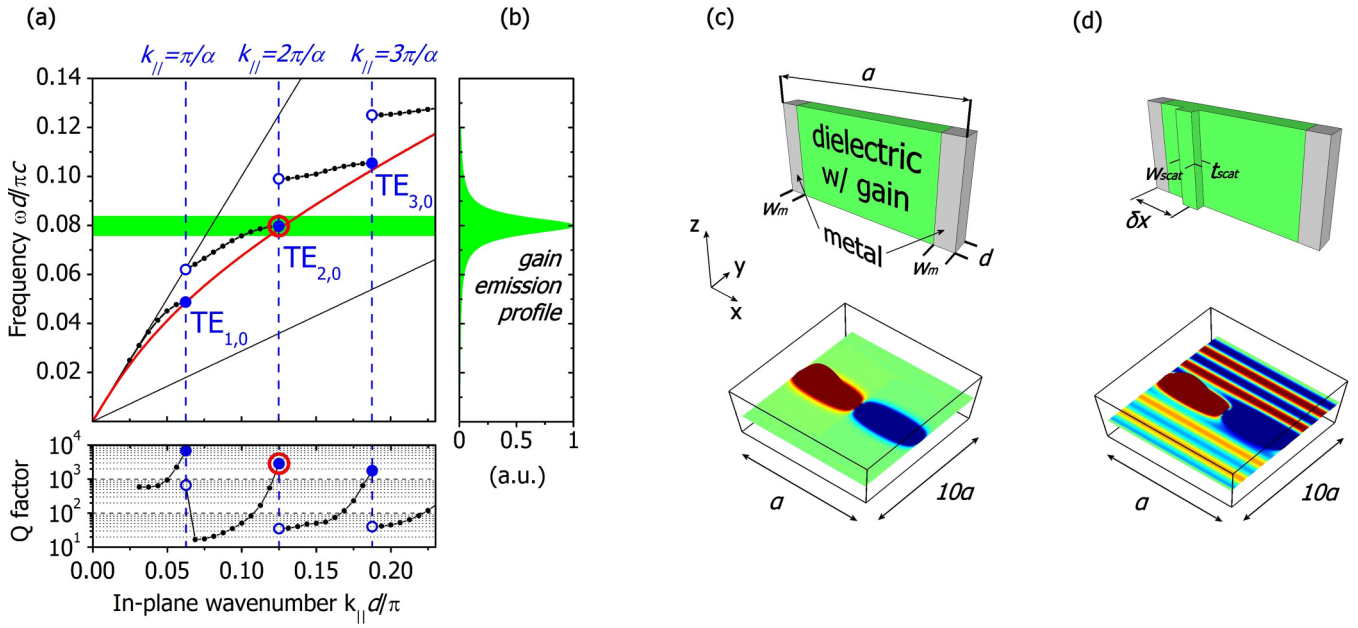

FIG. 1. The dark-mode laser principle of operation. (a) Dispersion relation of the *unpumped* uniform dielectric slab of thickness d (red line) and band structure of the composite dielectric-metal system (connected dots). The shaded area depicts the linewidth of the gain material and the red circle marks the operation point. The Q factor of each mode is also shown below. (b) Spectral emission profile of gain material, located at the frequency of the desired operation point. (c) Perspective view of a single unit cell without the scatterer (top) and lasing snapshot (bottom). (d) Perspective view of the same unit cell with the scatterer incorporated (top) and lasing snapshot (bottom). When pumped above the lasing threshold, the system lases into the dark mode as observed in both (c) and (d), but the stored power can be outcoupled only with the aid of a scatterer as in (d). The unit cell is periodically repeated along the x and z directions, forming an infinite radiating metasurface.

the scatterer. In contrast to other bright mode configurations where channeling of the lasing power into a neighboring dark mode is dentrimental [27], in our case the dark mode is the cornerstone. In order to implement the resonator, we choose a thin dielectric slab that supports a continuous dark bound state [red line in Fig. 1(a)] and then introduce silver scatterers of the same thickness d with a certain periodicity a. The purpose of the silver inclusions is to spatially quantize the modes of the dielectric slab, in order to tailor the desired mode distribution within the unit cell and to achieve a discrete set of resonant dark states. In essence, the dispersion of the composite metal-dielectric system becomes a quantized version of that of the dielectric slab, with periodicity π/a. In fact, as with any periodic system, the strong interaction of counterpropagating waves at the edge of the Brillouin zone leads to mode splitting and band structure formation [Fig. 1(a)]. The modes that are located at the bottom of each gap [blue dots in Fig. 1(a)] overlap with the metal inclusions at field minima (nodes) and have therefore significantly higher Q factors than their π-shifted counterparts that are located at the top of each gap [open blue dots in Fig. 1(a)] and overlap at field maxima. When the metal coincides with field maxima, the modes are repelled from the continuous dispersion line, due to strong scattering, while the opposite happens when the overlap happens at field minima. The slight deviation of the latter—high Q—modes from the continuous waveguide mode dispersion is due to the deviation of the effective permittivity of the composite metal-slab system from that of the pure dielectric slab.

Depending on the branch of the dispersion, an isolated mode with the desired operation frequency and spatial distribution can be chosen for operation. Here, we choose for simplicity the second of the quantized $TE_0^{(even)}$ modes [red circle in Fig. 1(a)], which has an antisymmetric electric field profile with respect to the center of the slab [Fig. 1(c)] and is therefore dark (in general any higher-order nonradiative mode is suitable). Choosing the operating wavelength to be within typical telecommunication ranges of 1.5 μm, the lattice constant of the unit cell is designed to be $a = 960$ nm and the width of silver $2w_m = 100$ nm. The overall thickness of the metasheet is $d = 60$ nm, which is thin enough to be subwavelength and can accommodate a gain material, such as a single quantum well [28,29]. The gain material is chosen to have an emission bandwidth centered at the desired operation frequency, as depicted in Fig. 1(b). The gain material is embedded in the dielectric of host permittivity $\varepsilon_{r,\mathrm{host}} = 12.1$ and the system is examined via self-consistent finite-difference time-domain (FDTD) calculations (see Appendix for details on the four-level gain system and the simulations). When the gain material is pumped adequately, i.e., above the lasing threshold, the dark mode is excited, as shown in Fig. 1(c), with macroscopic photon population such that predominantly stimulated emission into this dark mode takes place (lasing), but the electromagnetic power remains stored in the mode (only one unit cell shown here) because dissipative loss in the dielectric is low and radiative damping is suppressed as the mode is dark. Then, a dielectric scatterer of the same permittivity with dimensions $w_{\mathrm{scat}} = 60$ nm and $t_{\mathrm{scat}} = 30$ nm is placed on the surface with its center at distance δx from the unit cell boundary, as shown in Fig. 1(d), and the stored power can be now outcoupled as E_z-polarized

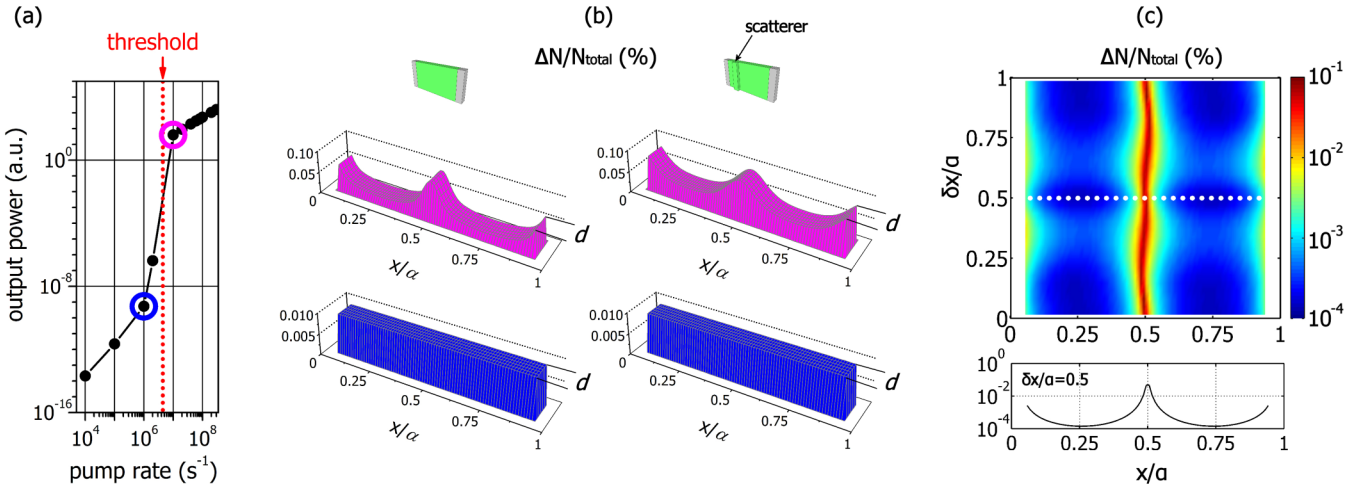

FIG. 2. Lasing simulations. (a) Lasing curve. The color code of the marked points corresponds to the population inversions shown in (b). (b) Population inversion ΔN (percentage % over N_{total}) in linear scale. Top row: above threshold [$R_p = 10^7\,\text{s}^{-1}$, magenta circle in (a)]. Bottom row: below threshold [$R_p = 10^6\,\text{s}^{-1}$, blue circle in (a)]. Left column: system without scatterer. Right column: system with scatterer placed at $\delta x = 150$ nm ($\delta x/\alpha \cong 0.16$). (c) Population inversion ΔN (percentage % over N_{total}) above threshold ($R_p = 10^9\,\text{s}^{-1}$) in logarithmic scale. (Top) Scanning the scatterer's position. The horizontal axis (x/α) corresponds to the unit cell and the vertical axis ($\delta x/\alpha$) to the scatterer's displacement. (Bottom) Plot of the cross-section marked in top figure, corresponding to a system with scatterer placed exactly in the middle of the unit cell.

waves [18], with a controllable small amount of radiative damping.

In each FDTD simulation, we pump the system at a certain pump rate R_p, wait until steady state is reached (∼50 ps) and then we sample the output in time domain and calculate the output power. Then we change the pump rate, repeat the procedure and eventually construct the lasing curve, as shown in Fig. 2(a). In the simulations the gain material is pumped homogeneously and therefore, after the population exchange between the four levels has reached equilibrium, the population inversion is constant throughout the gain material volume. This can be seen in Fig. 2(b) (bottom row), where the pump rate is set to be below threshold at $R_p = 10^6\,\text{s}^{-1}$ [the lasing threshold $R_p = 4.4 \times 10^6\,\text{s}^{-1}$ is marked with the red dotted line in Fig. 2(a)]. These figures [as well as all plots in Figs. 2(b) and 2(c)] show the population inversion $\Delta N = N_2 - N_1$ as percentage (%) over N_{total}, which is the sum of the total population contained in all four levels. The left panel in Fig. 2(b) corresponds to the system without the scatterer and the right one to the system with the scatterer placed at $\delta x = 150\,\text{nm}\,(\delta x/a \cong 0.16)$, but both figures are identical (bottom row), since below the lasing threshold all modes experience the same gain and the presence or not of the scatterer does not affect the system. However, when the gain material is pumped with $R_p = 10^7\,\text{s}^{-1}$, which is well above the lasing threshold for both systems, the lasing mode dominates among all other modes and modifies the gain material according to its particular field spatial distribution. That is, at areas within the gain material where the electric field is more intense, more energy is transferred to the mode and the gain material at those areas becomes more depopulated. In essence, ΔN maps the spatial distribution of the lasing mode, as can be seen in the top row of Fig. 2(b). Notice that because the gain slab is very thin compared to the dark mode extent, the depopulation is almost constant along the y axis. From these figures it is also evident that in the presence of the scatterer the depopulation is slightly weaker. The reason is that the onset of radiation damping, due to the scatterer, weakens the dark mode, reducing the Q factor and E-field amplitude inside the gain material. The presence of the scatterer slightly deforms the dark mode and, depending on its position, the electric field distribution depopulates the gain material accordingly. This can be seen in Fig. 2(c), where the scatterer's position is scanned and cross sections in the middle of the slab along the x axis are taken for each displacement δx. In this case, the gain material is pumped at even higher rate ($R_p = 10^9\,\text{s}^{-1}$) and, as a result, the contrast between the populated and depopulated regions of the gain material is stronger [notice that Fig. 2(b) is depicted in linear scale, while Fig. 2(c) is in logarithmic scale].

In Ref. [18], we demonstrated how the properties of the system change, depending on where the scatterer is situated with respect to the intensity profile of the dark mode. In brief, when the scatterer is either absent or placed exactly in the middle of the unit cell, then there is no radiative loss and all supplied power is converted to Joule heating at the metallic scatterers [Fig. 3(c)]. At this latter position where the output power is minimized (middle of unit cell), the lasing threshold acquires the minimum possible value for this specific design. The Q factor is maximized, with a maximum value limited only by the dissipative losses of the metal, which is calculated for realistic materials and dimensions to be $Q = 3{,}020$. As the scatterer is shifted along the unit cell, the coupling strength between the dark mode and radiation changes according to the shape of the dark mode; at positions where the fields are stronger, the coupling is more intense and hence the radiation damping stronger and the Q factor weaker [Fig. 3(b)]. The lasing threshold, which is also inherently related to the Q factor, is tuned accordingly [Fig. 3(d)]. An important aspect of this laser implementation is the directionality, which is achieved as the scatterer is shifted along the unit cell [Fig. 3(e)] (for further details see Ref. [18]).

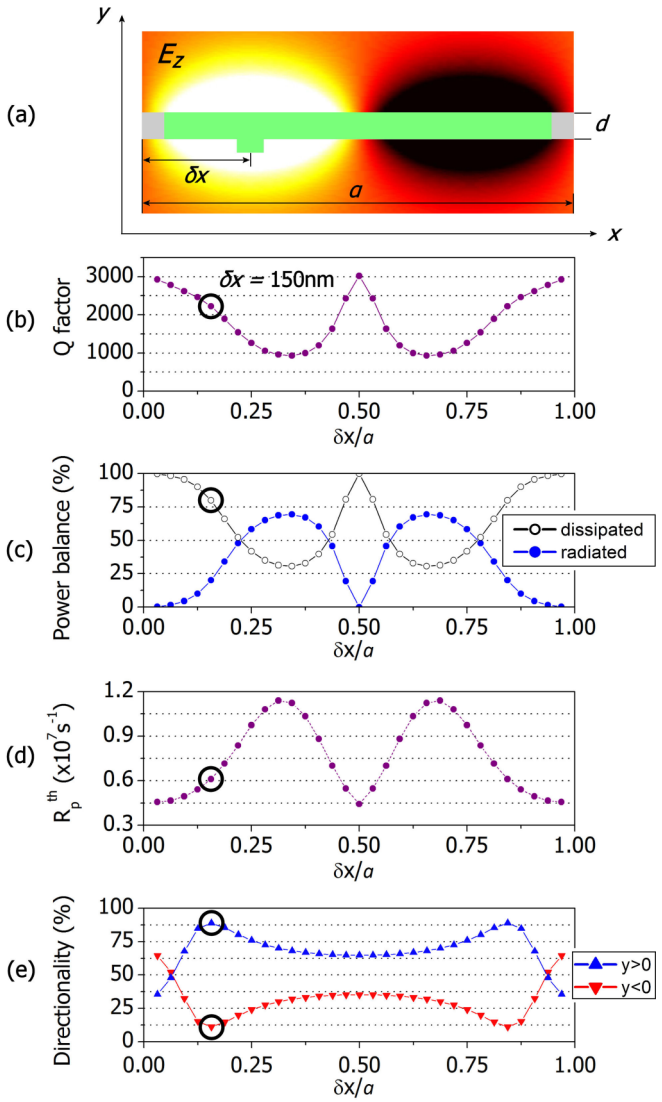

FIG. 3. Scanning the position of the scatterer (normalized with the unit cell width a). (a) Top view of unit cell, also showing the E_z spatial distribution of the dark mode. (b) Q factor. (c) Radiated and dissipated power over supplied power. (d) Lasing threshold. (e) Power emitted towards $y > 0$ (blue triangles pointing up) and $y < 0$ (red triangles pointing down), as the scatterer is shifted along the unit cell of the configuration described in Fig. 1. The marked displacement $\delta x = 150$ nm ($\delta x/a \cong 0.16$), corresponds to the configuration for which lasing simulations are shown in Fig. 2, striking a balance between field enhancement (Q factor), out-coupling, and achievable directionality. Notice that at $\delta x/a = 0.5$, the Q factor is the maximum possible for this configuration (Q factor of the dark mode) and is limited only by the losses due to the metal. At this position, the lasing threshold is the lowest possible and all lasing power, which cannot be radiated, is channeled to the metallic scatterers.

III. EFFECT OF LOSS CHANNELS

The energy that is stored in the dark mode by the pumping mechanism is subsequently removed from the system via either dissipative losses due to material absorption or radiation damping due to coupling of the oscillating mode to radiating waves. Ideally, in the total absence of these two energy loss channels, if energy is transferred into the dark mode it will be stored there indefinitely. However, in practice, not only is there inevitable absorption due to the metal, but also outcoupling is necessary for the stored energy to be delivered elsewhere.

In realistic implementations, reduction of the total loss is always desirable, because the lower the loss, the stronger the dark mode E field. Since gain is proportional to $|E|^2$, this means that much more gain can be achieved and hence, much more energy production inside the sample is possible for the same pump energy. In turn, the radiated power can be effectively larger, the exact level of which will be the result of the balanced effect of both loss channels. To identify the individual effect of each loss channel on the radiated power, the Q factor of the system can be decomposed into its two constituents, as: $1/Q = 1/Q_{\text{dissipated}} + 1/Q_{\text{radiated}}$, where each of the subscripts denotes the respective loss channel. $Q_{\text{dissipated}}$ can be boosted by choosing less lossy materials and Q_{radiated} can be boosted either by placing the scatterer close to the middle of the unit cell, as already seen in Fig. 3(b), or by making the scatterer weaker. The latter can be achieved if a material of lower permittivity is used or if the volume of the scatterer is made smaller (or simply the cross-section, for the two-dimensional case examined in this paper). All approaches above result in weaker polarization currents on the scatterers and hence weaker induced moments and weaker radiation (see Sec. VI for details). To examine the effect of each loss channel, we change the metal loss and the scatterer's strength individually. In our system we have used a Drude silver of permittivity $\varepsilon(f) = 1 - f_p^2/(f^2 - if\Gamma_p)$, with $f_p = 2181 \times 10^{12}$ 1/s and $\Gamma_p = 4.74 \times 10^{12}$ 1/s, based on Johnson and Christy (JC) data [30,31] and a scatterer of permittivity $\varepsilon_{r,\text{scat}} = 12.1$ and dimensions $w_{\text{scat}} = 60$ nm and $t_{\text{scat}} = 30$ nm. To modify the losses of the JC silver we simply tune Γ_p, thus modifying $Q_{\text{dissipated}}$ and to change the scatterer's strength, we either change the permittivity $\varepsilon_{r,\text{scat}}$ or the width w_{scat}, thus modifying Q_{radiated}. Although all modifications can be imposed simultaneously, we make one change at a time on the original system. The results of the parametric study are shown in Fig. 4. For each scenario, the radiated power is shown in the last column as a percentage (%) over the generated power. To identify which loss channel is responsible for each change in the output power, Q_{radiated}, $Q_{\text{dissipated}}$ as well as the total Q factor are also shown in the first, second, and third columns, respectively. In the top row the metal loss is varied among $\Gamma_p = 0.1$ THz (artificial low-loss metal), 4.74 THz (JC silver) and 10 THz (artificial high-loss metal). In the middle row, the scatterer's permittivity is varied among $\varepsilon_{r,\text{scat}} = 4$ (e.g., HfO_2), 12.1 (e.g., Si) and 30 (artificial high-ε_r material). Last, in the bottom row, the scatterer's width is varied among $w_{\text{scat}} = 30$, 60, and 90 nm.

In Fig. 4, it is evident that the metal losses affect the dissipative part of the Q factor, while the outcoupling affects the radiative part of the Q factor, as expected. The radiated power follows the combined action of both and can be seen in the fourth column of Fig. 4; in each panel the radiated power, expressed as a percentage (%) over the generated power, changes inversely with the total Q factor. This trend reflects the way the actual outcoupled power changes, when the generated power is the same for all systems. However, as already mentioned, the generated power can differ significantly from system to system. In fact, this is expected even within

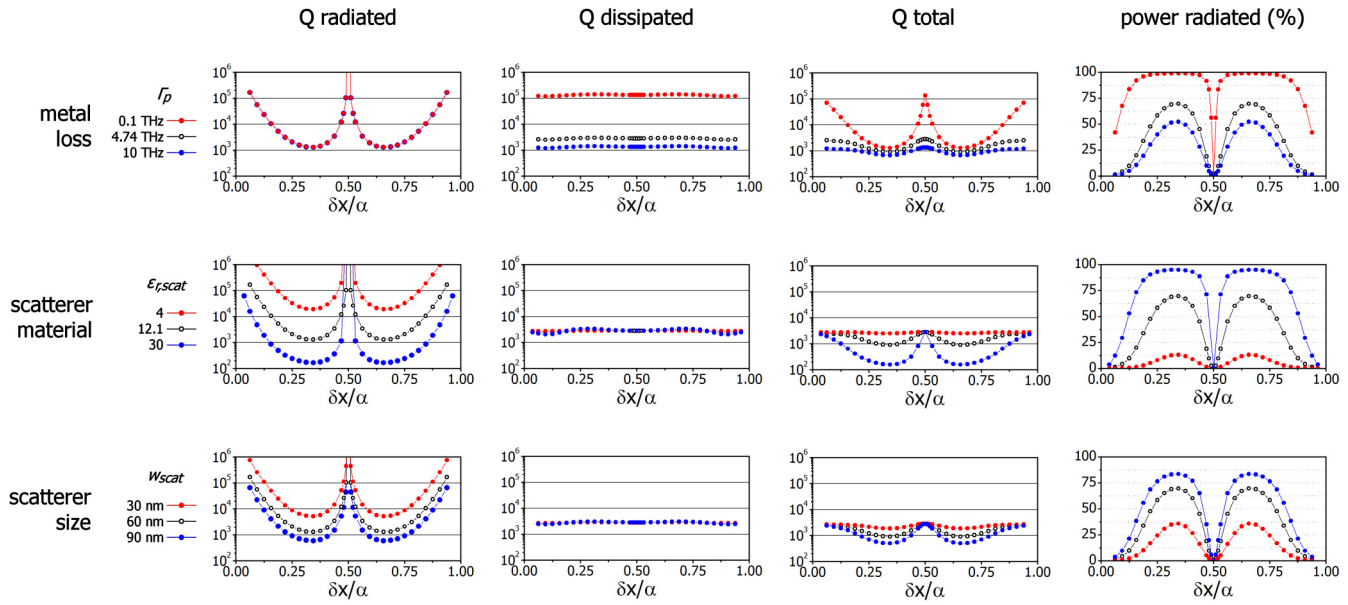

FIG. 4. Effect of loss channels on Q factor and radiated power. The radiated power is expressed as a percentage (%) over the generated power and changes inversely with the total Q factor.

a single system, as already implied by Fig. 2 where the gain material depopulation was shown to depend on the scatterer's position. It is therefore necessary to examine in absolute units how the radiated power is modified as the scatterer is shifted and as the materials change. Next, we scan the metal loss for two families of systems, one bearing a scatterer with $\varepsilon_{r,\mathrm{scat}} = 12.1$ and one with $\varepsilon_{r,\mathrm{scat}} = 30$. All systems are pumped at the same pump rate $R_p = 10^9\ \mathrm{s}^{-1}$, so as to ensure that the input power spent on each system is equal. The results are presented in Fig. 5.

Indeed, from any individual data set shown in Figs. 5(b) and 5(e), it is evident that in a certain system more power is generated when the scatterer is placed so as to minimize radiation damping, i.e., at positions where the dark mode is weak. Among different systems, more power is generated for combinations of materials that minimize both loss channels (for the cases studied, that would correspond to $\varepsilon_{r,\mathrm{scat}} = 12.1$ and $\Gamma_p = 0.1$ THz, i.e., red dots in Fig. 5(b)). Both conclusions are intuitively interpreted if one observes the peak value $|E|$ of the dark mode [Figs. 5(a) and 5(d)]. Configurations that sustain

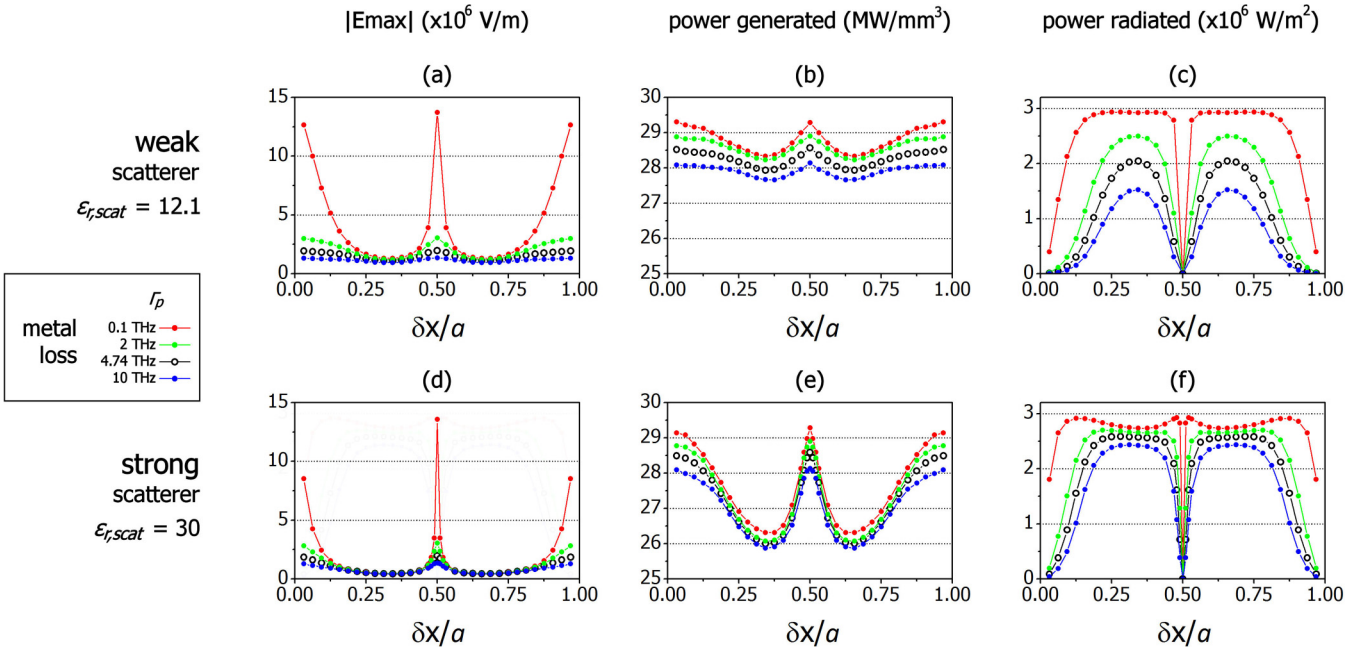

FIG. 5. Effect of loss channels on [(a) and (d)] amplitude of dark mode, [(b) and (e)] generated power, and [(c) and (f)] radiated power. The permittivity of the scatterer is set to $\varepsilon_{r,\mathrm{scat}} = 12.1$ in (a)–(c) and $\varepsilon_{r,\mathrm{scat}} = 30$ in (d)–(f). The metal loss is set to $\Gamma_p = 0.1,\ 2,\ 4.74$, and 10 THz. The combinations of $\varepsilon_{r,\mathrm{scat}}$ and Γ_p are chosen to span a wide range of cases.

TABLE I. Properties of popular gain materials. The columns contain information about the emission wavelength (λ_{emit}), emission cross-section (σ_e), concentration (N), gain coefficient ($\gamma = \sigma_e N$), refractive index of host material (n_{host}), and the reference from which the information has been retrieved.

Gain medium		λ_{emit} (nm)	σ_e (cm^2)	N (cm^{-3})	γ (cm^{-1})	n_{host}	Reference
Solid State	ruby	694	2.5×10^{-20}	1.58×10^{19} atoms	0.4	~1.76	[32,33]
	Nd:YAG	1064	2.8×10^{-19}	1.4×10^{20} atoms	39	1.82	[32,33]
	Yb:Er:Glass (phosphate)	1540	0.8×10^{-20}	10×10^{20} atoms	8	1.53	[32]
	Ti : Al_2O_3	790	3.4×10^{-19}	3.3×10^{19} atoms	11	~1.76	[32,33]
	Er^{+3} (in glass)	1550	2×10^{-20}	5×10^{19} atoms	1	1.45	[34,35]
Dye	Rh. 800 (in methanol)	710	2.65×10^{-16}	6×10^{18} molecules	1590	~1.32	[14,36]
	Rh. 6G (in methanol)	560	3×10^{-16}	3×10^{18} molecules	900	~1.34	[37]
	Rh. 6G (in ethanol)	570	2×10^{-16}	6×10^{16} molecules	12	~1.36	[38]
	PM597 (in polymer)	580	8×10^{-17}	6×10^{15} molecules	0.48	~1.5	[39]
Quantum Dots	CdSe (in UV glue matrix)	593	2.34×10^{-15}	3.7×10^{15} QDs	9	1.54	[40]
	PbSe (in UV gel)	1580	3×10^{-16}	3×10^{15} QDs	0.9	1.46	[41]
Quantum Well	InGaAs/InGaAsP	1500	–	–	5000	~3.8	[42]
	InGaAsN/InP	1570	–	–	2500	~4	[43]

stronger fields produce more power for the same input power (pump). On the other hand, the amount of the power that is finally radiated depends on the trade-off between the two loss channels. This is why more output with less generated power is possible as well, if one compares the systems denoted with open dots in Figs. 5(b), 5(c) and 5(e), 5(f), for example.

The trade-off between the two loss channels is even more evident if one observes the system shown in red dots in Fig. 5(f) (i.e., the narrow peak in radiated power in the immediate vicinity of the center position of the scatterer ($\delta x/a = 0.5$) where the radiative coupling goes to zero); as the scatterer is directed towards the center or the edge of the unit cell, radiation damping becomes weaker and leads the system to increase the Q factor, hence to produce more energy and effectively outcouple more. After some point, though, the internal losses dominate, leading the system to reduce and saturate the Q factor (Fig. 4), hence to saturate the energy production inside the sample and reduce the output power.

IV. ESTIMATION OF REALISTIC MATERIAL GAIN (ANALYSIS RELATED TO POPULATIONS N_2 AND N_1)

To estimate the amount of gain that is needed for our system to lase, we need to translate our threshold calculations into material gain. The material gain coefficient $\gamma(\mathrm{m}^{-1})$, which is usually the typical quantity considered in realistic implementations, is given by [4]

$$\gamma = \frac{4\pi}{\lambda}\mathrm{Im}(\sqrt{\varepsilon_{r,\mathrm{gain}}}), \tag{1}$$

where λ is the free-space wavelength. On the other hand, our calculations are performed in terms of pump rate $R_p(\mathrm{s}^{-1})$, which is a parameter very closely connected to the quantum nature of our four-level gain system; it merely tells us the rate at which electrons are raised from the ground energy level N_0 to the upper level N_3. After the electrons are excited at level N_3, they start a downward return route to the ground state N_0, through levels N_2 and N_1. If level N_2 is filled from N_3 faster than it is depleted, then the population difference $\Delta N = N_2 - N_1$ can be positive (population inversion) and energy is transferred from the gain material to the fields (emission), while the opposite (absorption) happens when $\Delta N < 0$. The population difference ΔN in the quantum gain system is expressed classically as an averaged polarization density [44]. This polarization density is then connected with the electric field in terms of a pump-dependent susceptibility $\chi_{\mathrm{gain}}(R_p)$ and the total material permittivity due to the host and the embedded gain material is $\varepsilon_{r,\mathrm{gain}}(R_p) = \varepsilon_{\mathrm{host}} + \chi_{\mathrm{gain}}(R_p)$. The gain permittivity $\varepsilon_{r,\mathrm{gain}}$ is therefore the connecting link between R_p and γ. For our four-level gain system, γ is given by (see Appendix for derivation)

$$\gamma = \frac{4\pi}{\lambda}\mathrm{Im}\left[\sqrt{\varepsilon_{r,\mathrm{host}} + i\frac{\sigma_a}{\varepsilon_0\omega_a\Gamma_a}\frac{\tau_{30}(\tau_{21}-\tau_{10})R_p}{\tau_{32}+\tau_{30}[1+R_p(\tau_{10}+\tau_{21}+\tau_{32})]}N_{\mathrm{total}}}\right]. \tag{2}$$

In this expression, the dark mode frequency is assumed to be aligned with the gain emission frequency, as it actually is in our case. The general expression that takes frequency mismatch into account can be found in Appendix.

To give an estimate for the order of magnitude of typical gain coefficients γ and a guide for potential experimental implementations, some popular gain materials are listed in Table I. The values shown have been retrieved from the references shown in the last column and fall within the typical range for each material.

In our case, the gain material is embedded in the slab and hence $\varepsilon_{r,\mathrm{host}} = 12.1$ (for the other parameters appearing in Eq. (2) see Appendix). Using the parameters of our simulations the lasing threshold shown earlier in Fig. 3(d) in terms of pump

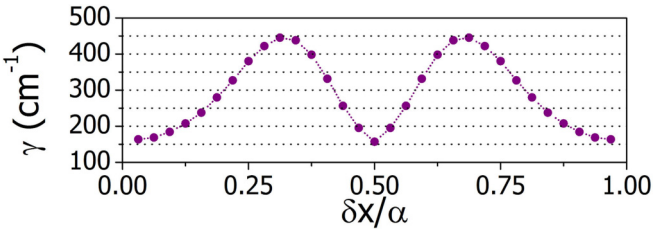

FIG. 6. Lasing threshold of system shown in Fig. 1(d), in terms of material gain coefficient γ, corresponding to the data already presented in Fig. 3(d) in terms of pump rate.

rate R_p is now converted into material gain γ, as shown in Fig. 6. We see that for the loss channels assumed in our model, the gain ranges between $160 - 450\,\mathrm{cm}^{-1}$, which is typically within realistically achievable values as indicated by Table I.

V. PUMPING EFFICIENCY (ANALYSIS RELATED TO POPULATIONS N_3 AND N_0)

To estimate the pumping efficiency we need to calculate how much of the power that we provide to the system in order to achieve lasing is actually received by the system and not channeled elsewhere. In our simulations the gain is pumped homogeneously, corresponding to carrier injection, as in typical semiconductor lasers. An internal loss channel has been included via τ_{30} in our model for the gain material, but, other than that, it is assumed that all pumped energy is delivered to the atoms and consumed to induce transitions and hence the pump rates discussed so far correspond to a 100% quantum yield (QY). If $QY < 1$, then in order to find the overall pumped power that is spent on the system (and partly delivered to the atoms), the calculated threshold pump rate can be corrected by division with QY.

On the other hand, if gain is pumped optically, i.e., by means of an incident optical beam, then the system's response becomes also involved. In this case the pump beam is partly absorbed by the gain material (which is embedded in the host) and a fraction of the absorbed optical power is then consumed to induce the atomic transitions (expressed via QY), while the rest is converted to other forms (phonon vibrations, etc). Hence, the actual power that is transferred to the atoms will be the product $QY \times A$, where A is the absorptance. The knowledge of A is therefore crucial, as it can indicate preferable spectral regions to pump the gain material. In other words, the efficiency will strongly depend on the spectral overlap of the pump beam with the system's response, which is defined both by the bulk material properties of the constituents, as well as by their geometry.

As for the bulk properties, the gain material absorbs at higher frequencies than it emits, as basic quantum mechanics dictate [44], and hence there are spectral regions above the lasing frequency where $\mathrm{Im}(\varepsilon_{r,\mathrm{gain}})$ is negative. The absorptance depends on the bulk absorption coefficient, which for the gain material is expressed as $\alpha = \frac{4\pi}{\lambda}\mathrm{Im}(\sqrt{\varepsilon_{r,\mathrm{gain}}})$, where the imaginary part of $\varepsilon_{r,\mathrm{gain}}$ is now negative, as it accounts for absorption and not gain. In practice the absorptive $\varepsilon_{r,\mathrm{gain}}$ is related to $N_3 - N_0$ (and not to $N_2 - N_1$ as in γ) as $\alpha = \sigma_A(N_3 - N_0)$, where σ_A is the atomic absorption cross-section [32]. Because the number of electrons at the ground level is immense, usually $N_3 \ll N_0$ and $\alpha \cong -\sigma_A N_0 < 0$.

Besides the bulk properties of gain, the absorptance depends on geometric considerations as well; the gain material is structured in a system with a certain spectral response and, as such, enhanced absorption at certain spectral regions could be favored, thus increasing the pumping efficiency. In order to get an estimate of such a possibility we overlook for the moment the detailed response of the gain material and we model absorption in the gain region with a constant positive imaginary part in the slab's permittivity $\varepsilon_{r,\mathrm{host}}$. Noticing that the absorption cross-section σ_A is a property of the gain material, while the population difference $N_3 - N_0$ depends on the pump rate (effectively on the pump beam intensity), a whole family of gain materials and pump intensities are considered under a certain value of $\mathrm{Im}[\varepsilon_{r,\mathrm{host}}]$.

For gain materials suitable to our configuration, such as dyes [14,36], the absorption cross-sections and dye concentrations vary within the ranges $\sigma_A \sim (10^{-16} - 10^{-15})\,\mathrm{cm}^2$ and $N \sim (10^{18} - 10^{19})\,\mathrm{cm}^{-3}$, which translate into $\mathrm{Im}(\varepsilon_{r,\mathrm{host}}) \sim (10^{-3} - 10^{-1})$. Within this range, we next measure A in the metal and in the dielectric separately (Fig. 7). Assessing only the total A might be misleading because it results from absorption both in the gain and in the metal and should be therefore calculated separately in each region. Pumping can be realized in the spectral range 200–400 THz, located just above the $\mathrm{TE}_{2,0}$ dark mode with which our system lases. When the beam is directed at normal incidence, the wavefronts that advance towards the metasheet impose the same phase to all unit cells. Consequently the beam cannot couple to odd-order modes such as $\mathrm{TE}_{3,0}, \mathrm{TE}_{5,0}$ etc., which require a π shift among neighboring unit cells. However, even-order modes such as the $\mathrm{TE}_{2,0}$ and $\mathrm{TE}_{4,0}$ bright modes [open circles in Fig. 1(a)], i.e., those modes that radiate without the need of any scatterer, fulfill the phase requirements. The $\mathrm{TE}_{4,0}$ dark mode is located in the same spectral region, but requires a scatterer to couple. For our calculations we remove the scatterer and, hence, the dark $\mathrm{TE}_{4,0}$ mode does not appear in the spectrum as expected, but the bright $\mathrm{TE}_{2,0}$ and $\mathrm{TE}_{4,0}$ modes are present. As seen in Fig. 7, at those modes the absorptance in the gain material gets significantly increased and hence they are preferable spectral regions for pumping. Notice how the absorbed power transfers from the metal to the gain region with increasing $\mathrm{Im}(\varepsilon_{r,\mathrm{host}})$.

VI. DIRECTIONALITY

In Ref. [18], we demonstrated how directional emission can be controlled in our system with the aid of two scatterers and how it can be achieved even with a single scatterer. Due to the deeply subwavelength thickness of the laser, directionality can be explained in a straightforward manner via an equivalent electromagnetic current sheet. In brief, if we consider an infinite current sheet which radiates exactly as our system, then the emission of such a sheet can be controlled by an appropriate mixture of an electric $\mathbf{j_e}$ and a magnetic $\mathbf{j_m}$ current. The equivalent boundary conditions for the current sheet are $\hat{\mathbf{n}} \times (\mathbf{E_2} - \mathbf{E_1}) = -\mathbf{j_m}$, $\hat{\mathbf{n}} \times (\mathbf{H_2} - \mathbf{H_1}) = \mathbf{j_e}$, where $\hat{\mathbf{n}}$ is the surface normal of the current sheet pointing from region 1 to region 2. In the actual system, the dark mode oscillates along the z axis and produces z-polarized waves and, hence,

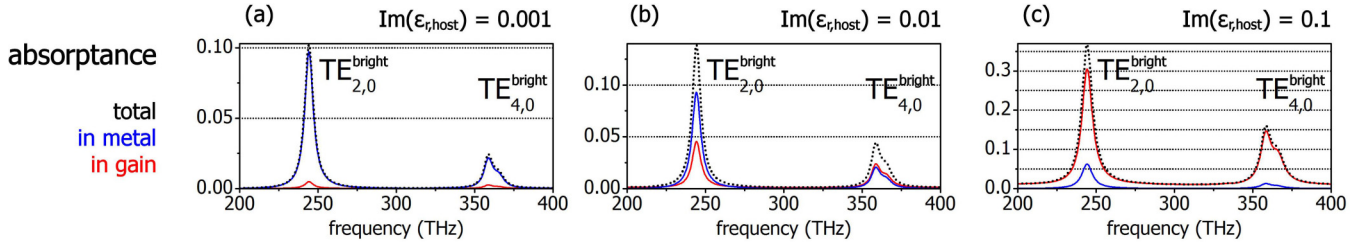

FIG. 7. Absorptance in gain (red line), in metal (blue line), and total absorptance (black line) for the system in Fig. 1(c) (normal incidence). Gain material with (a) $\mathrm{Im}(\varepsilon_{r,\mathrm{host}}) = 10^{-3}$, (b) 10^{-2}, and (c) 10^{-1}, modeling three families of absorption cross-sections and pump intensities. Notice how absorptance increases with increasing $\mathrm{Im}(\varepsilon_{r,\mathrm{host}})$ and how the absorbed power transfers from the metal to the gain region with increasing $\mathrm{Im}(\varepsilon_{r,\mathrm{host}})$.

in the equivalent sheet model it is assumed that $\mathbf{j_e} = j_e\hat{\mathbf{e}}_\mathbf{z}$ and $\mathbf{j_m} = j_m\hat{\mathbf{e}}_\mathbf{x}$, with $(\hat{\mathbf{e}}_\mathbf{x},\hat{\mathbf{e}}_\mathbf{y},\hat{\mathbf{e}}_\mathbf{z})$ denoting the Cartesian unit vector set. Consequently, after applying the boundary conditions, the outgoing electric and magnetic fields are expressed as

$$\mathbf{E}^{\pm} = E_z^{\pm}\hat{\mathbf{e}}_\mathbf{z} = -\tfrac{1}{2}(\eta j_e \pm j_m)e^{i(\omega t \mp ky)}\hat{\mathbf{e}}_\mathbf{z} \tag{3a}$$

and

$$\mathbf{H}^{\pm} = H_x^{\pm}\hat{\mathbf{e}}_\mathbf{x} = \pm\frac{1}{\eta}E_z^{\pm}\hat{\mathbf{e}}_\mathbf{x}, \tag{3b}$$

respectively, and the time-averaged Poynting vector along each side of the current sheet is

$$\begin{aligned}\langle\mathbf{S}\rangle &= \frac{1}{2}\mathrm{Re}(\mathbf{E}^{\pm}\times\mathrm{conj}(\mathbf{H}^{\pm})) = \langle S\rangle^{\pm}\hat{\mathbf{e}}_\mathbf{y}\\ &= \pm\frac{1}{8\eta}\left(|\eta j_e|^2 + |j_m|^2 \pm 2|\eta j_e||j_m|\cos\left(\delta\varphi_{j_e,j_m}\right)\right)\hat{\mathbf{e}}_\mathbf{y},\end{aligned} \tag{4}$$

where $\delta\varphi_{j_e,j_m}$ is the phase difference between $\mathbf{j_e}$ and $\mathbf{j_m}$, η the surrounding space impedance and the sign $\pm$ denotes the respective direction of emission along the y axis.

Each one of the currents alone emits symmetrically to both sides of the sheet [set $\boldsymbol{j}_e = 0$ or $\boldsymbol{j}_m = 0$ in Eq. (4), for example], but with a balanced contribution the sheet can be made purely directional, i.e., emitting only to one side. Imposing fully directional power flow on Eq. (4) leads to the condition $|\eta j_e| = |j_m|$ for the amplitude of the equivalent currents and $\delta\varphi_{j_e,j_m} = 0$ (emission along $y > 0$) or $\delta\varphi_{j_e,j_m} = \pi$ (emission along $y < 0$) for their relative phase difference.

In order to implement this concept with the actual system, the lasing mode has to be coupled simultaneously to an electric and a magnetic moment and this can be achieved by introducing an additional weak scatterer on the opposite side of the slab. In essence, the dark mode will induce polarization currents I_1 and I_2 on the two scatterers, which subsequently radiate. These individual currents can be interpreted as a weighted mixture of a symmetric $I_S \sim I_2 + I_1$ and an antisymmetric $I_\mathrm{A} \sim I_2 - I_1$ current of the combined double-scatterer system, i.e., as a weighted mixture of an electric moment and a magnetic moment that radiate individually (Fig. 8). Depending on the phase and amplitude of each moment, their superposition can enhance or cancel radiation along a certain direction according to Eq. (4). In practice, the two contributions can be tuned by coupling each scatterer with different parts of the dark mode, i.e., simply by shifting the position of the scatterers. Hence, the amplitude and phase of I_1 and I_2 change, I_S and I_A are modified accordingly and directionality is in effect controlled by the position of the scatterers.

To gain better insight, let us employ a simple model to relate the equivalent quantities j_e and j_m to the actual polarization currents I_1 and I_2 that run the scatterers. Since the unit cell is periodically repeated along the x axis, the actual system can be replaced by an effective medium which radiates exactly as the original system, consisting of an infinite homogeneous slab with an array of currents I_1 on one side and an array of currents I_2 on the other side. In essence, the dark mode and the scatterers are replaced by current wires. Whatever amplitude and phase I_1 and I_2 inherit from the dark mode is attributed to the wires and therefore the slab does not need to bear the metal stripes anymore. The sparse wires can be further replaced with equivalent infinite electric current sheets of appropriate surface current densities J_1 and J_2, as shown in Fig. 9.

The electromagnetic problem now consists of two radiating infinite current sheets and, in order to relate them to the equivalent electric and magnetic currents, their currents J_1 and J_2 can be again expressed as a superposition of a symmetric J_S and an antisymmetric J_A current, i.e., as $J_1 = J_S + J_A$ and $J_2 = J_S - J_A$. The sheets are separated by a distance d and divide space into three homogeneous regions, characterized by permittivities $\varepsilon_{r,1}$, $\varepsilon_{r,2}$, and $\varepsilon_{r,3}$, which correspond to regions 1, 2, and 3, respectively, as shown in Fig. 9. Application of the boundary conditions on each interface yields the fields in all three regions. Assuming the slab is embedded in a uniform environment, i.e., $\varepsilon_{r,1} = \varepsilon_{r,3} \triangleq \varepsilon_{\mathrm{out}}$, where $\varepsilon_{\mathrm{out}}$ is the

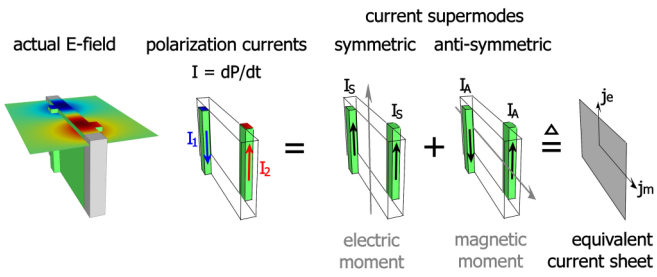

FIG. 8. Directionality explained via the equivalent current sheet model. The dark mode induces polarization currents I_1 and I_2 on the two scatterers, which are effectively a weighted mixture of an electric moment and a magnetic moment that radiate individually. These moments are equivalently described by an infinite electromagnetic current sheet supporting an electric current j_e and a magnetic current j_m.

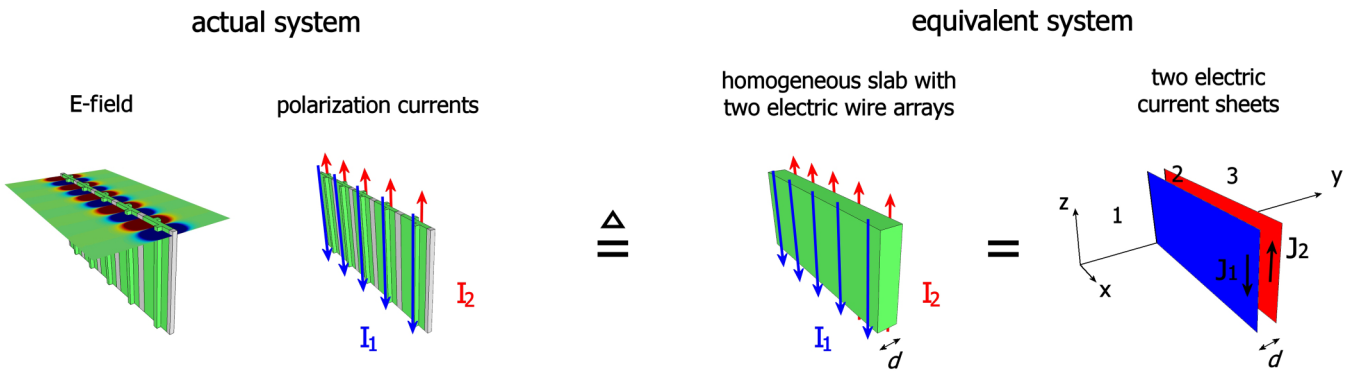

FIG. 9. The double current sheet model. The composite system is replaced by a homogeneous region of thickness d between two electric current sheets which represent the polarization currents running through the scatterers.

permittivity surrounding the slab, the electric field in regions 1 and 3 is given in terms of J_S, J_A, by (see Appendix for details):

$$\mathbf{E}^{\pm} = -\left(\eta J_S \frac{2re^{-ik_2d} + (e^{-ik_2d})^2(r-1) + (r+1)}{-(e^{-ik_2d})^2(r-1)^2 + (r+1)^2} \pm \eta J_A \frac{2re^{-ik_2d} - (e^{-ik_2d})^2(r-1) - (r+1)}{-(e^{-ik_2d})^2(r-1)^2 + (r+1)^2}\right) \times e^{i(\omega t \mp ky)}\hat{\mathbf{e}}_{\mathbf{z}}, \quad (5)$$

where $k_2 = n_2\frac{\omega}{c}$, n_2 is the refractive index in region 2 (slab index) and $r \triangleq \frac{\eta}{\eta_2} = \sqrt{\frac{\mu}{\varepsilon_{\text{out}}}}/\sqrt{\frac{\mu}{\varepsilon_{r,2}}} = \sqrt{\frac{\varepsilon_{r,2}}{\varepsilon_{\text{out}}}}$. The wave impedances η and η_2 correspond to the surrounding environment and to region 2, respectively.

Comparing this result with Eq. (3a) from the equivalent currents, it is easy to notice that

$$\frac{1}{2}\eta j_e = \left(\eta \frac{2re^{-ik_2d}(e^{-ik_2d})^2(r-1) + (r+1)}{-(e^{-ik_2d})^2(r-1)^2 + (r+1)^2}\right) J_S \quad (6a)$$

and

$$\frac{1}{2} j_m = \left(\eta \frac{2re^{-ik_2d} - (e^{-ik_2d})^2(r-1) - (r+1)}{-(e^{-ik_2d})^2(r-1)^2 + (r+1)^2}\right) J_A. \quad (6b)$$

What is of importance to our study is not the absolute quantities j_e and j_m, but their relative amplitude and phase and hence we may use Eqs. (6a) and (6b) to write their ratio as

$$\frac{\eta j_e}{j_m} = \frac{2re^{-ik_2d} + (e^{-ik_2d})^2(r-1) + (r+1)}{2re^{-ik_2d} - (e^{-ik_2d})^2(r-1) - (r+1)} \frac{J_S}{J_A}. \quad (7)$$

This ratio is a product of a term due to the currents (J_S/J_A) and a term originating from the intermediate space (region 2). From this expression it is evident that a phase acquired from the slab is added to the phase lag between J_S, J_A. In the absence of the slab, $r = 1(\varepsilon_{r,2} = \varepsilon_{\text{out}})$ and the result (7) simplifies to

$$\frac{\eta j_e}{j_m} = i\cot(k_2 d/2)\frac{J_S}{J_A}, \quad (8)$$

revealing that there is always a $\pi/2$ phase shift between $\delta\varphi_{J_S,J_A}$ and $\delta\varphi_{j_e,j_m}$, which denote the phase lag between J_S and J_A and between j_e and j_m, respectively.

Given the fact that every part of the dark mode oscillates coherently, I_1 and I_2 that run the scatterers can be driven either in phase (if both are scatterers placed either at $\delta x > a/2$ or $\delta x < a/2$) or π-out of phase (if one is placed at $\delta x > a/2$ and the other at $\delta x < a/2$). In effect, J_1 and J_2 are excited likewise, as well as their linear combinations J_S and J_A. Consequently, $\delta\varphi_{J_S,J_A}$ is either 0 or π and, hence, in the absence of the slab, the equivalent currents would oscillate with a $\pm\pi/2$ phase lag, as Eq. (8) reveals. Under these circumstances, the system would radiate equally to both sides, regardless of the individual amplitude of $\eta j_e, j_m$ [set $\delta\varphi_{j_e,j_m} = \pm\pi/2$ in Eq. (4) for example], i.e., regardless of the exact position of the scatterers. In practice, although the scatterers are indeed driven either in phase or π-out of phase, an additional phase lag is provided by the material in between, i.e., the slab, as predicted by the result (7). The dielectric slab is made from a polarizable material and hence its width and permittivity affect the directionality. When the slab is present $\delta\varphi_{j_e,j_m}$ can be calculated from Eq. (7):

$$\delta\varphi_{j_e,j_m} = \overbrace{\arctan\left(\frac{2r}{(r^2-1)\sin(k_2 d)}\right)}^{\delta\varphi_{\text{slab}}} + \delta\varphi_{J_S,J_A}. \quad (9)$$

This result indicates that, for finite n_2 (as in real materials), $|\delta\varphi_{\text{slab}}|$ has a nonzero lower bound $|\delta\varphi_{\text{slab}}|_{\min}$ whenever $\sin(k_2 d) = \pm 1$ and an upper bound $|\delta\varphi_{\text{slab}}|_{\max}$ if $r = 1$ (absence of slab) or $\sin(k_2 d) = 0$. Given that $\delta\varphi_{J_S,J_A} = 0$ or π, $|\delta\varphi_{\text{slab}}|_{\max}$, which is $\pi/2$, leads to $\delta\varphi_{j_e,j_m} = \pm\pi/2$ and consequently to a 50%-50% power split. This we have already encountered when the slab is absent. On the other hand, $|\delta\varphi_{\text{slab}}|_{\min}$ translates into an upper bound for the directionality, as for fully directional power flow, besides $|\eta j_e| = |j_m|$, it should be $\delta\varphi_{j_e,j_m} = 0$ or π, which Eq. (9) does not reach. This is not a surprise, as we have already observed in our system [Fig. 3(e)].

Note that these conclusions are the same whether we use one or two scatterers, as we can always relate the actual polarization currents to effective J_S and J_A. Using the parameters of our system, $\varepsilon_{\text{out}} = 1$, $\varepsilon_{r,2} = 12.1$, $\omega = 2\pi \times 200$ THz, and $d = 60$ nm, we find $\delta\varphi_{j_e,j_m} = 0.218\pi$, which agrees with the numerically calculated value 0.22π, as presented in Fig. 10(a). The slight observed detuning results from the dark mode frequency detuning within the range 195–200 THz, as the position of the scatterer changes. In the same figure, we also show how the amplitudes of the equivalent currents vary

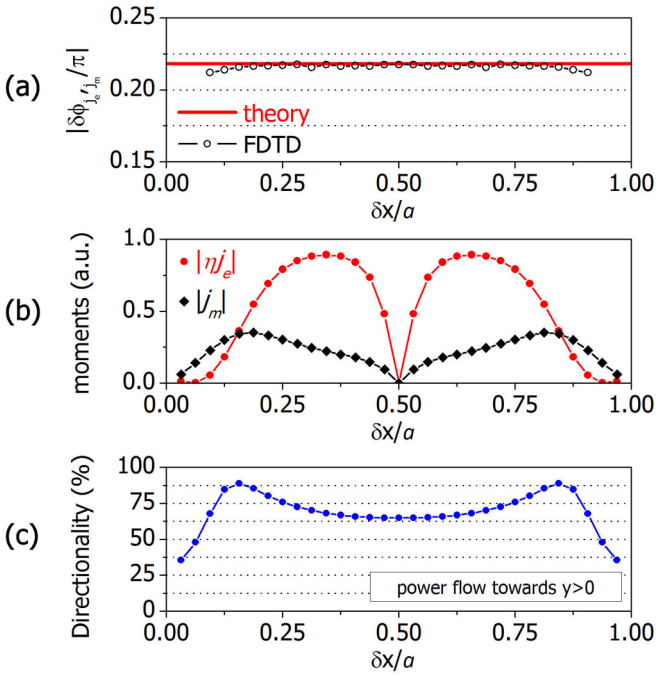

FIG. 10. Directionality examined via the equivalent current sheet model. (a) Phase lag between the equivalent currents j_e and j_m. Connected open circles: calculated numerically from the phase and amplitude of emitted fields during lasing (the variation is within numerical error). Red solid line: theoretical result as calculated with the double current sheet model. (b) Numerically calculated $|\eta j_e|$ and $|j_m|$. (c) Directionality reproduced from Fig. 3(e). Notice that directionality is maximized at those scatterer's positions where $|\eta j_e| = |j_m|$.

as the scatterer is shifted along the unit cell. The resulting directionality towards $y > 0$ is also reproduced from Fig. 3(e), to emphasize the fact that it becomes maximum whenever $|\eta j_e| = |j_m|$, although not 100% because of the phase residue.

For the parameters of our system, it is $\sin(k_2 d) \cong 0.8 < 1$ and hence directionality can be further improved. In order to find this upper bound, we set $|\eta j_e| = |j_m|$ and in Eq. (4), which gives $|\langle S\rangle^{\pm}| / (|\langle S\rangle^{+}| + |\langle S\rangle^{-}|) = \pm\frac{1}{2}(\cos(\delta\varphi_{j_e,j_m}) \pm 1) \times 100\%$ for the fraction of the power flow towards $y > 0$ (choose $+$) or $y < 0$ (choose $-$). Using Eq. (9), we find that $|\delta\varphi_{\text{slab}}|_{\min}$ translates into a maximum directionality of $\pm\frac{1}{2}[\cos(\arctan(\frac{2r}{r^2-1}) + \delta\varphi_{J_S,J_A}) \pm 1] \times 100\%$. For $\varepsilon_{\text{out}} = 1$ and $\varepsilon_{r,2} = 12.1$, we find $\delta\varphi_{j_e,j_m}{}^{\min} = 0.178\pi$, which translates into a 92.4%–7.6% maximum power split, directed either towards $y > 0$ for $\delta\varphi_{J_S,J_A} = 0$ or towards $y < 0$ for π [see Fig. 11(b)]. This can be achieved in practice if the slab width is increased to $d = 108$ nm, for example, as can be seen in Fig. 11. In order to keep the dark mode frequency at 200 THz, the unit cell size should be reduced accordingly. In Figs. 11(a) and 11(b), we plot for $\varepsilon_{\text{out}} = 1$ corresponding to our system, as well as for $\varepsilon_{\text{out}} = 2$ and 4 are presented, modeling the case where the slab is located in between a substrate and a superstrate of the same material. The double current sheet model predicts reduction of the maximum directionality in this case.

If the unit cell length remains constant ($a = 960$ nm) as d changes, then the dark mode frequency shifts as well and, as a rule of thumb, drops as the slab width increases. In Fig. 11(c), this combined effect is examined via FDTD simulations for several slab widths (the results correspond to Fig. S5, supplementary material in Ref. [18]). Comparison with the double current sheet model is also shown, where both contributions have been taken into consideration, showing very good agreement. It should be noted that the restriction on directionality is a consequence of deriving both electric and magnetic sheet currents nonresonantly from the same dark mode, locking their relative phase; for independent $\mathbf{j_e}$ and $\mathbf{j_m}$, perfect directionality is possible.

The apparent limitation of our system results from the fact that the scatterers were for simplicity chosen to be nonresonant. In practice, many techniques can be used to alter the phase between j_e and j_m. To achieve $\delta\varphi_{j_e,j_m} = 0$ and boost directionality to the maximum, one could take control over the phase delay by making the scatterers resonant. Cut wires, either dielectric or metallic [45], strips made out of nanoparticles

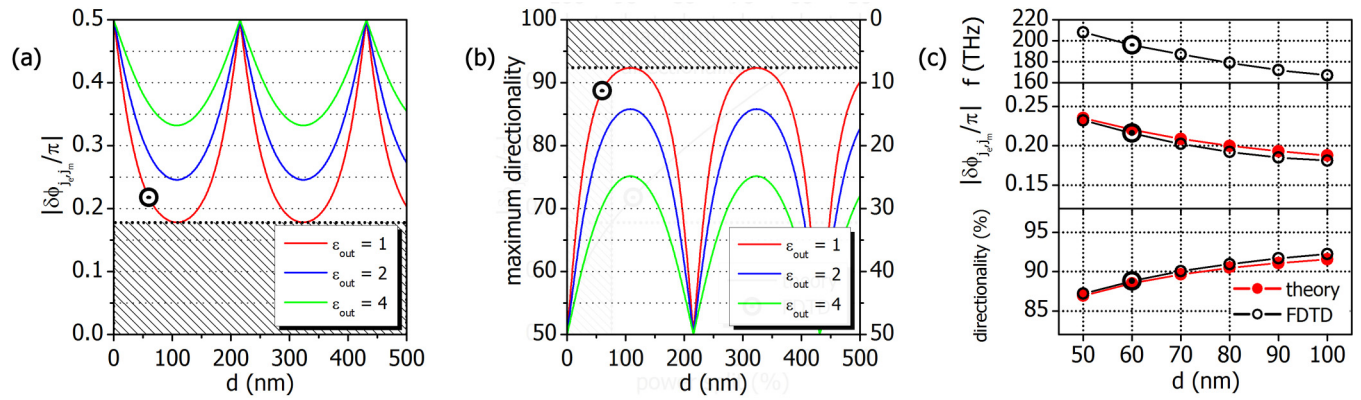

FIG. 11. Directionality examined via the double current sheet model. (a) Phase lag between the equivalent currents j_e and j_m and (b) maximum directionality, as a function of the slab width d, for $\varepsilon_{\text{out}} = 1,2$, and 4 ($f = 200$ THz, i.e., constant). The horizontal dotted line marks the minimum and the marked circle corresponds to our system for $d = 60$ nm and $\varepsilon_{\text{out}} = 1$. (c) Effect of slab width on the phase lag between the equivalent currents j_e and j_m (middle panel) and directionality (bottom panel) as predicted by the double current sheet model (red dots) and calculated with the FDTD (black circles) for $\varepsilon_{\text{out}} = 1$. The dark mode frequency shifts (top panel), because the unit cell is kept constant at $a = 960$ nm, contrary to (a) where the frequency was kept constant (implying resizing of the unit cell length as d changes). Our system for $d = 60$ nm is marked with a dotted circle, as also shown in (a) and (b).

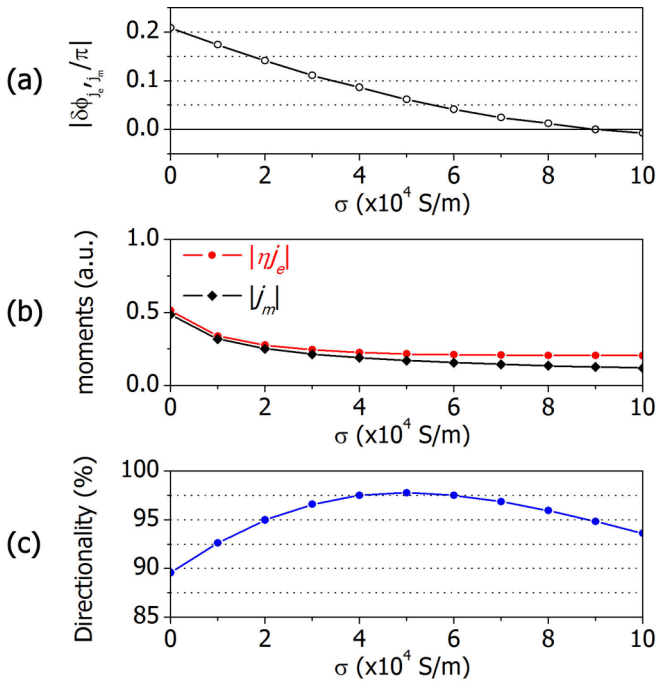

FIG. 12. Boosting directionality by making one scatterer lossy. (a) Phase lag between equivalent currents, (b) amplitudes of equivalent currents and (c) directionality, as the conductivity of the scatterer is increased.

with a specific plasmon resonance or Mie resonant objects like spheres periodically placed on the surface are just a few examples. Dielectric implementations have the advantage of low loss, but even with metallic resonant objects, one does not need to be exactly on the resonance where the absorption is maximized to achieve the necessary phase.

This general concept can be demonstrated indirectly, still with our simple configuration, via the introduction of loss in the scatterers. The permittivity is now written as $\varepsilon_{r,\mathrm{scat}} = \varepsilon'_{r,\mathrm{scat}} + i\varepsilon''_{r,\mathrm{scat}}$ and the loss tangent $\tan\delta = \varepsilon''_{r,\mathrm{scat}}/\varepsilon'_{r,\mathrm{scat}}$ which expresses the relative phase between E and J is controlled via $\varepsilon''_{r,\mathrm{scat}}$ or the corresponding conductivity $\sigma = \omega\varepsilon''_{r,\mathrm{scat}}$. In Fig. 12, we show how $|\eta j_e|$, $|j_m|$, and $\delta\varphi_{j_e,j_m}$ change as we artificially introduce conductivity to one of the scatterers, without changing their position. Their initial positions are such that $|\eta j_e| = |j_m|$ (point C in Fig. 5 of Ref. [18]) and as the conductivity increases, the phase lag between the moments reduces, until it becomes zero for $\sigma = 9 \times 10^4$ S/m. The loss tangent for this conductivity gives $\delta \cong 0.2\pi$, which matches the residue phase $\delta\varphi_{j_e,j_m} = 0.218\pi$. The directionality, nevertheless, does not reach a maximum there, because the amplitudes of the moments are detuned. Instead, the maximum is reached earlier for $\sigma = 5 \times 10^4$ S/m and it is in fact a $97.8\% - 2.2\%$ power split.

VII. ALTERNATIVE PLANAR IMPLEMENTATIONS

A. Laser system on a substrate and gain material embedded in dielectric slab

In a practical implementation, the metasheet would be fabricated on a certain substrate, which also serves as a mechanical support. The presence of the substrate causes a shift in the mode frequency, which can be taken into account during the system design, and also extends the evanescent tails of the mode into the new material region. In order to induce the least possible reduction of the mode amplitude in the gain region, it is preferable that the refractive index of the substrate is significantly lower than that of the metasheet. In this way the interaction of the gain material with the dark mode can be maintained as strong as possible.

To illustrate this possibility, we consider here a system designed on a substrate, which is assumed to be a glass of typical permittivity $\varepsilon_{r,\mathrm{sub}} = 2.1$. The system incorporates the gain material in the dielectric region of the metasheet (Fig. 13), exactly as the systems examined so far. In our configuration, the mode frequency decreases with increasing substrate thickness and converges after approximately 800 nm; hence we assume a substrate of 1000 nm. Instead of adjusting the unit cell size in order to avoid the change in the operation frequency, as perhaps in a real design situation, we prefer to keep the same design in order to examine the effect of the additional material on the system. In order to eliminate any contribution from the possible detuning with the gain material emission frequency ω_α, we tune ω_α to coincide with the new operation frequency, which now is $\omega_\alpha = 2\pi \times 185$ THz.

In Fig. 13, we examine this scenario and demonstrate the case when the scatterer is located in the substrate region (top row), as well as in the air region (bottom row). The calculations indicate that no dramatic changes occur. The Q factor is slightly enhanced for the major range of the scatterer's displacement, except for regions around its maxima, where a slight drop is observed; this variation affects the ratio of the radiated over the supplied power, accordingly. As for the power split between the two directions of emission, the additional material causes a slight drop in the maximum directionality, as also predicted previously by the double current sheet model (Fig. 11). This is due to the fact that the refractive index step between the dielectric slab and its surroundings has become smaller, but can in principle be compensated by considering materials of different width and/or permittivity.

B. Laser system on a substrate and gain material as a superstrate

On the other hand, the gain material does not necessarily need to be located inside the dielectric slab. Because of the deeply subwavelength thickness of the slab, a significant part of the dark mode's energy is located just outside the slab, i.e., within the evanescent tails of the bound state. This, in fact, can be beneficial, since it allows for the gain material to be placed as a superstrate on top of the existing system. In this way the strong near field of the bound state can be used as a means of interaction with the gain system, a mechanism which could otherwise not be feasible if the mode confinement was too strong, as in typical semiconductor laser systems [4]. It is noteworthy that in those systems the very same feature would be detrimental.

To illustrate this second possibility, we consider here a system designed on a substrate, which is assumed to be a glass of typical permittivity $\varepsilon_{r,\mathrm{scat}} = 2.1$. This time the gain medium is placed on top of the metasheet (Fig. 14) and the host

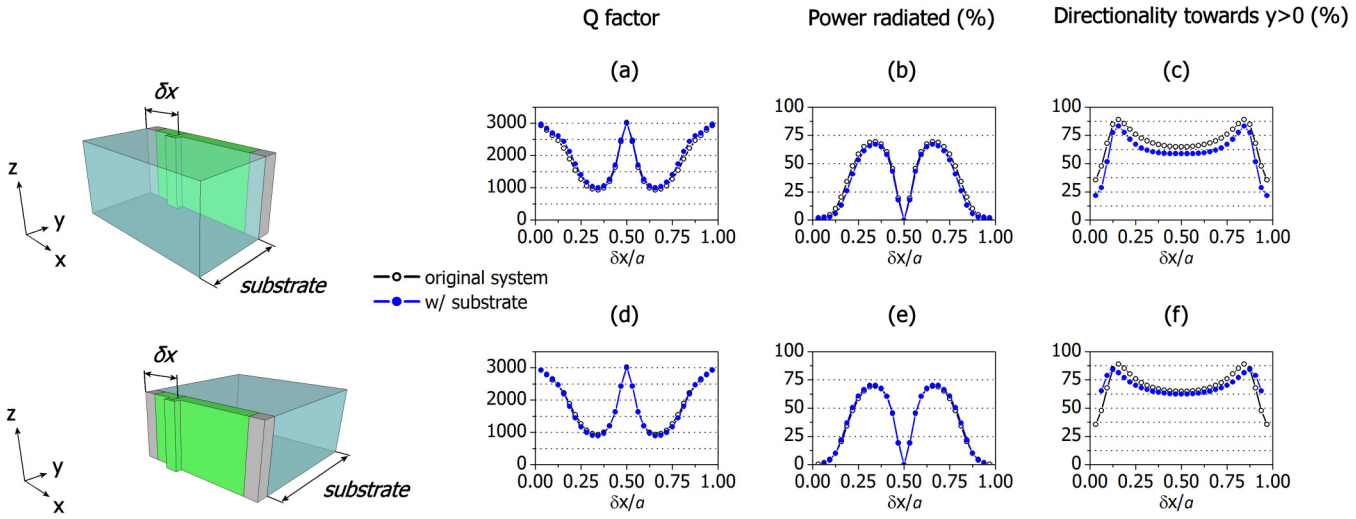

FIG. 13. Metasurface laser system placed on a glass substrate of thickness 1 μm, with gain medium embedded in the dielectric slab. (a)–(c) Scatterer placed in the substrate region. (d)–(f) Scatterer placed in the superstrate region. [(a) and (d)] Q factor. [(b) and (e)] Radiated over supplied power. [(c) and (f)] Power emitted towards $y > 0$ for both systems. The results of Fig. 3 are reproduced here as open symbols, for easier comparison.

permittivity is considered to be $\varepsilon_{r,\text{host}} = 2.25$, which is close to typical fluorescent dye systems [14,46], certain polymer systems [47] or quantum dots dispersed in a thick PMMA layer [48,49]. The gain layer is 200 nm thick to ensure a sufficient overlap with the mode tails (the mode intensity extends over a total of 164 nm FWHM along the y axis). As previously, in order to eliminate any contribution from the possible detuning with the gain material emission frequency ω_α, we tune ω_α to coincide with the new operation frequency of each system, namely $\omega_\alpha = 2\pi \times 176$ THz.

Again the calculations indicate that no dramatic changes occur. Interestingly, though, covering the metasheet with material on both sides induces an almost constant 70%–30% power split, for most positions of the scatterer [Fig. 14(c)]. In practice, the Q factor and consequently the lasing threshold can be tuned independently of the directionality for a wide range of choices.

The option to embed the gain material either in the slab or on top can be very handy in practical situations where the choice of the gain material is limited, either by availability or by the desired operation frequency. Semiconductors, such as quantum wells [28,29] and quantum dots [48,49], usually emit in the infrared region, while dyes emit in the visible [14,36,46] and incorporating each material into a photonic structure

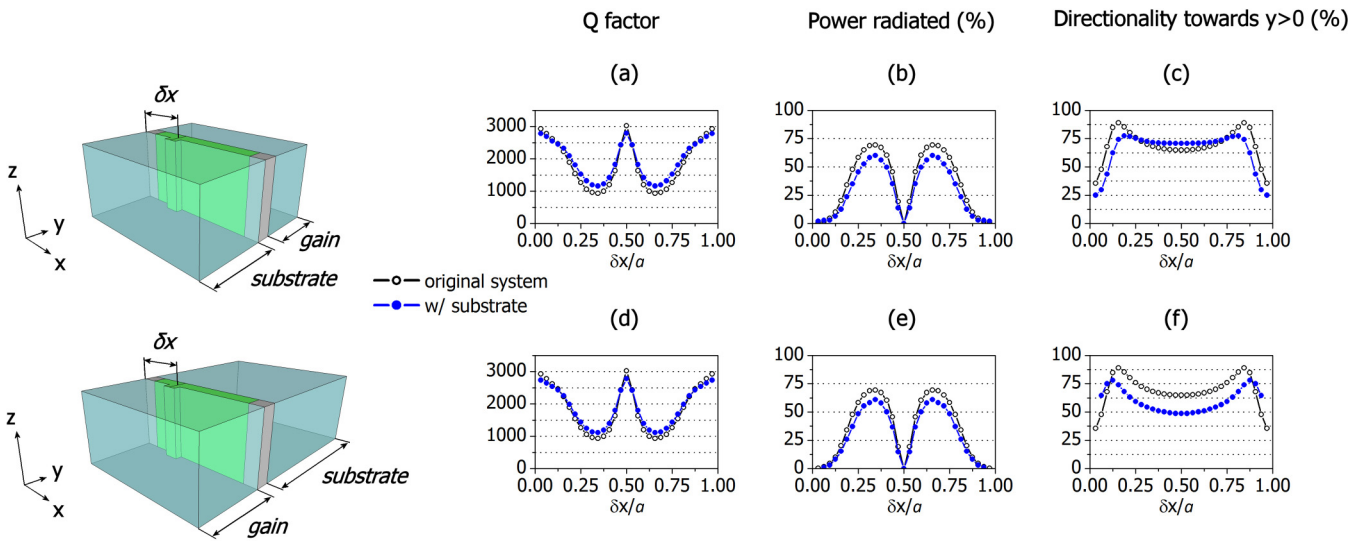

FIG. 14. Metasurface laser system placed on a glass substrate of thickness 1 μm, with gain medium of thickness 200 nm placed on top of the dielectric slab. (a)–(c) Scatterer placed in the substrate region. (d)–(f) Scatterer placed in the superstrate region. (a) and (d) Q factor. (b) and (e) Radiated over supplied power. (c) and (f) Power emitted towards $y > 0$ for both systems. The results of Fig. 3 are reproduced here as open symbols, for easier comparison.

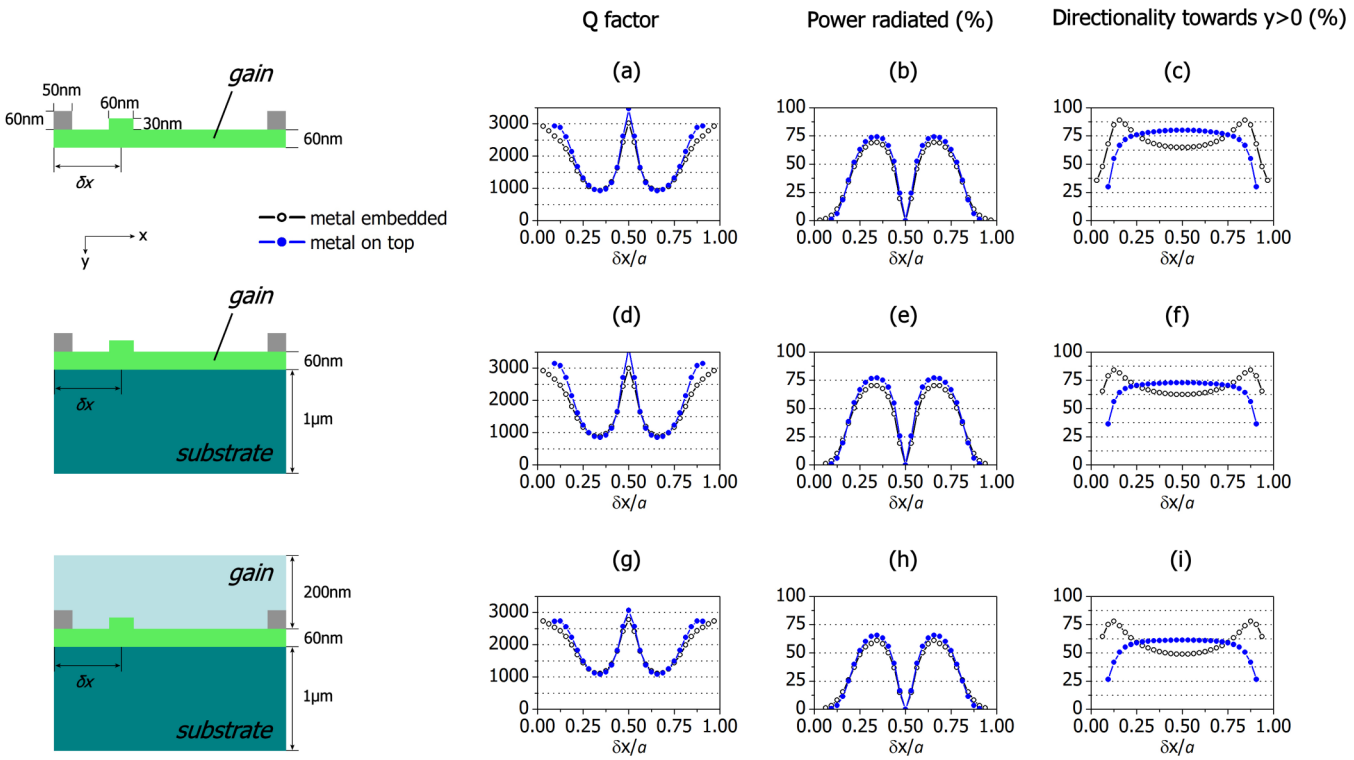

FIG. 15. Metal stripes placed on top of the slab, enabling fully layer-by-layer fabrication. Metasurface laser system placed on a glass substrate of thickness 1 μm, with gain medium of thickness 200 nm placed on top of the dielectric slab. (a)–(c) System in air. (d)–(f) System on a substrate. (g)–(i) System on a substrate with gain layer on top. (a), (d), (g) Q factor. (b), (e), (h) Radiated over supplied power. (c), (f), (i) Power emitted towards $y > 0$. The open symbols correspond to each respective system, when the metal is embedded in the slab.

may differ. Quantum wells can serve as the slab itself, while quantum dots can be placed as a superstrate. Similarly, dyes or quantum dots which can be embedded in a polymer matrix can be placed as a superstrate. In general, the gain material must overlap as much as possible with the dark mode and hence, depending on the spatial extent of the dark mode, the best choice for the location of the gain material will also depend on the refractive index step between the slab and the substrate.

C. Metal stripes on top of the dielectric slab

If interrupting the dielectric slab with metal is not preferable in fabrication, the metal stripes can be deposited on top of the slab, as sketched in Fig. 15. Besides the theoretical case where the system is examined in air surroundings, inclusion of a substrate and a superstrate is again possible and a fully layer-by-layer fabrication is now enabled. To examine the properties of such systems, we consider metal bars of the same material and dimensions as previously and move them on top of the slab, filling the void area with dielectric. Interestingly, the nonsymmetric placement of the metal with respect to the slab repels the dark mode to the opposite side of the slab. The dark mode, which was previously squeezed between the metal bars, may now interact less with the metal and this effect is observed in Fig. 15 as an increase in the Q factor, for all three systems. In particular, when a substrate is added, the mode becomes even more asymmetric along the y axis, as it is attracted into the substrate area and the Q factor increases significantly [Fig. 15(d)]. Next, when a superstrate is added on top of the slab-substrate system, the mode asymmetry relaxes due to the balance of the surrounding refractive index and the Q factor drops [Fig. 15(g)]. In all cases, though, putting the metal on top of the slab, instead of embedding it in the dielectric, increases the Q factor, because of the geometric asymmetry, which induces an asymmetric mode profile. In effect, the output power increases. Interestingly, the deformation of the dark mode leads to a different pattern in directionality. It becomes almost flat for the major range of scatterer's displacement and the maximum directionality can be now achieved when the scatterer is placed as close to the metal as possible.

VIII. CONCLUSION

In this work, we examined the properties of the dark mode laser concept, implemented here in a planar configuration. The most important feature of this concept is the ability to control separately the power storing mechanism from outcoupling. Because of this feature, the same system can be used in alternative schemes. For laser applications, as in our case, outcoupling to free propagating modes is desired and necessary. But, alternatively, the lasing power can be outcoupled to surface waves that may exist in the substrate surface, rendering the system a laser source for surface plasmons. Outcoupling can even be completely suppressed. In this case, the dark mode laser will constitute a source of highly confined and very strong near fields, only limited by dissipation. This kind of source could be further used for applications where very strong local fields are necessary, as

for example to drive transitions in entities like biomolecules. Because the implementation is dielectric, our system can offer appreciably higher Q factors compared to other plasmonic systems. Of course, due to the inclusion of metals, as a realistic and easy means for quantizing the fields, some losses are inevitably introduced. However, we showed how the trade-off between loss and radiation damping can be controlled, thus allowing us to tailor the system to our needs. Depending on whether the goal is a low lasing threshold, a strong output or a selective direction of emission, the system can be tuned to deliver the desired properties. Most importantly, facilitating the fabrication in a fully layer-by-layer fashion does not sacrifice its properties, giving promise for future experiments.

ACKNOWLEDGMENTS

Work at FORTH (simulations) was supported by the European Research Council under the ERC Advanced Grant No. 320081 (PHOTOMETA). The work at Ames Laboratory (theory) was partially supported by the US Department of Energy (Basic Energy Science, Division of Materials Sciences and Engineering) under Contract No. DE-AC02-07CH11358.

APPENDIX

FDTD self-consistent calculations. The gain material is homogeneously embedded in the dielectric host medium, which has relative permittivity $\varepsilon_{r,\text{host}} = 12.1$, and is modeled as a four-level quantum system [44,50–55], as shown in Fig. 16. The pumping takes place between the ground state (N_0) and the third level (N_3) via the pumping rate R_p, which corresponds to electrical pumping as in typical semiconductor lasers [4]. The lasing action takes place between the second level (N_2) and the first level (N_1), which are called the *upper* and *lower lasing levels*, respectively. The rate equations that describe our model are

$$\frac{dN_3}{dt} = -\frac{1}{\tau_{32}}N_3 - \frac{1}{\tau_{30}}N_3 + R_p N_0, \tag{A1a}$$

$$\frac{dN_2}{dt} = +\frac{1}{\tau_{32}}N_3 - \frac{1}{\tau_{21}}N_2 + \frac{1}{\hbar\omega_a}\mathbf{E}\cdot\frac{\partial \mathbf{P}_a}{\partial t}, \tag{A1b}$$

$$\frac{dN_1}{dt} = +\frac{1}{\tau_{21}}N_2 - \frac{1}{\tau_{10}}N_1 - \frac{1}{\hbar\omega_a}\mathbf{E}\cdot\frac{\partial \mathbf{P}_a}{\partial t}, \tag{A1c}$$

$$\frac{dN_0}{dt} = +\frac{1}{\tau_{10}}N_1 + \frac{1}{\tau_{30}}N_3 - R_p N_0, \tag{A1d}$$

where the polarization density induced by the gain material is given by

$$\frac{\partial^2 \mathbf{P}_a}{\partial t^2} + \Gamma_a \frac{\partial \mathbf{P}_a}{\partial t} + \omega_a^2 \mathbf{P}_a = -\sigma_a (N_2 - N_1)\mathbf{E}. \tag{A2}$$

The gain medium is assumed to have a Lorentzian response which is homogeneously broadened with linewidth $\Gamma_\alpha = 2\pi \times 20 \times 10^{12}$ rad/s and emission frequency $\omega_\alpha = 2\pi \times 196 \times 10^{12}$ rad/s, except for the systems in Figs. 13 and 14, where $\omega_\alpha = 2\pi \times 185 \times 10^{12}$ rad/s and $\omega_\alpha = 2\pi \times 176 \times 10^{12}$ rad/s, respectively (ω_α is chosen to coincide with the operation frequency of each). The gain material is characterized by the lifetimes $\tau_{30} = 10$ ps, $\tau_{32} = 1$ ps, $\tau_{21} = 100$ ps, and $\tau_{10} = 0.1$ ps and the coupling constant is $\sigma_\alpha = 10^{-4}\,\text{C}^2/\text{kg}$. Silver is modeled by a Drude response $\varepsilon(\omega) = 1 - {\omega_p}^2/(\omega^2 + i\omega\gamma)$, with $\omega_p = 1.37 \times 10^{16}$ rad/s and $\gamma = 2.98 \times 10^{13}$ rad/s, and in all calculations the discrete time and space steps are set to $\delta t = 15 \times 10^{-18}$ s and $\delta x = 10 \times 10^{-9}$ m, respectively. In our FDTD simulations, the total electron density is considered to be $N_0(t=0) = N_0(t) + N_1(t) + N_2(t) + N_3(t) = 5 \times 10^{23}\,\text{m}^{-3}$ and the initial condition is that all electrons are in the ground state and all electric, magnetic and polarization fields are zero. Next, noise is inserted into the system and the electrons are homogeneously pumped from N_0 to N_3 with a constant pump rate R_p. Then, the system of the Maxwell equations coupled with the atomic rate equations is self-consistently solved and this procedure is repeated for several pump rates.

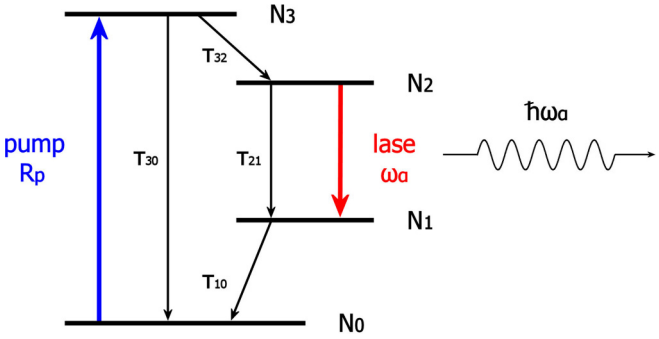

FIG. 16. Schematic of the four-level gain medium. Pumping takes place between the ground state (N_0) and the third level (N_3) via the pumping rate R_p and the lasing action takes place between the second level (N_2) and the first level (N_1). The nonradiative decay processes between the ith and jth energy levels are described by the $1/\tau_{ij}$ decay rates.

Pump-intensity calculation. The pumping rate is equivalent to pump intensity. The pump power density is equal to $\hbar\omega_a R_p N_0$, and the pump intensity $I_\text{p} =$ (pump power)/(surface area) $= \hbar\ \omega_a R_p N_0$ (volume)/(surface area) $= \hbar\ \omega_a R_p N_0 d$, and d is the thickness of the gain layer. If we use the numbers of our simulations, $R_p = 4.4 \times 10^6\,\text{s}^{-1}$, $N_0 = 5 \times 10^{23}\,\text{m}^{-3}$, $\omega_a = 2\pi \times 196\,\text{THz}$, and $d = 60$ nm, then $I_p = 0.017\,\text{W/mm}^2$.

Power-balance calculations. The supplied and dissipated power are calculated as a volume integral of the product $\mathbf{E}\,\text{d}\mathbf{P}/\text{dt}$, where $\mathbf{E}$ is the electric field and $\mathbf{P}$ the polarization density as calculated locally from the FDTD. Integration in the gain volume provides the supplied power and integration in the metal volume provides the dissipated power. Their difference is always equal to the time-averaged calculated Poynting vector, as verified for all cases considered.

Q factor calculations. For the calculation of the Q factor as $Q = \omega\tau$, we need to measure the photon lifetime τ (ω is the mode frequency). In the FDTD, an incident field of appropriate frequency ω excites a certain mode and once steady state has been reached, the incident field is set to zero. After some short transient time the system energy starts to decay exponentially as $\exp(-t/\tau)$ and the electric field as $\exp(-t/2\tau)$. Monitoring the electric field amplitude as a function of time, $E(t)$, the Q factor can be calculated from the slope of $\ln[E(t)]$, which is equal to $-1/2\tau$.

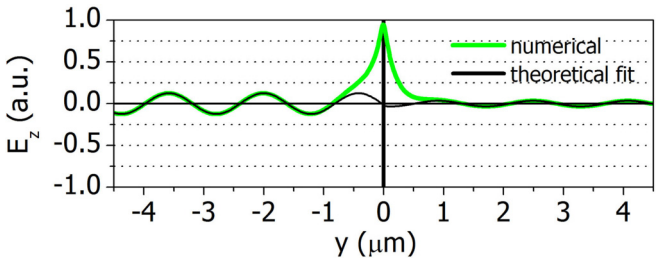

FIG. 17. Cross-section along the y axis of the electric field during a lasing simulation (snapshot at steady state) and theoretical fit of the outgoing waves.

Directionality calculations. Directionality is calculated as the time-averaged Poynting vector of the emitted power on both sides of the metasheet, after lasing has reached steady state.

Phase and amplitude of equivalent currents. In order to calculate the equivalent currents we may work either with the E or the H field. After lasing has reached steady state we measure the outgoing field $F \in \{E,H\}$ along the y direction and retrieve the amplitude $F^{\pm}$ and phase $\delta\varphi_F^{\pm}$ of the field by a simple fit with $|F^{\pm}|\cos(\omega t \mp ky + \delta\varphi_F^{\pm})$ or in complex notation $F^{\pm}e^{i(\omega t \mp ky)}$, where $F^{\pm} = |F^{\pm}|e^{i\delta\varphi_F^{\pm}}$. Then we solve Eq. (3) in terms of the equivalent currents and separate the result into amplitudes and phases as $\eta j_e = |\eta j_e|e^{i\varphi_{j_e}}$ and $j_m = |j_m|e^{i\varphi_{j_m}}$. For example, for the electric field, we may write $E_z^{\pm}e^{i(\omega t \mp ky)} = -\frac{1}{2}(\eta j_e \pm j_m)e^{i(\omega t \mp ky)} \Rightarrow \begin{cases} \eta j_e = -E_z^+ - E_z^- \\ j_m = -E_z^+ + E_z^- \end{cases}$

$$\Rightarrow \begin{cases} |\eta j_e|e^{i\varphi_{j_e}} = -|E_z^+|e^{i\delta\varphi_E^+} - |E_z^-|e^{i\delta\varphi_E^-} \\ |j_m|e^{i\varphi_{j_m}} = -|E_z^+|e^{i\delta\varphi_E^+} + |E_z^-|e^{i\delta\varphi_E^-} \end{cases}$$

$$\Rightarrow \begin{cases} |\eta j_e| = |-|E_z^+|e^{i\delta\varphi_E^+} - |E_z^-|e^{i\delta\varphi_E^-}| \\ |j_m| = |-|E_z^+|e^{i\delta\varphi_E^+} + |E_z^-|e^{i\delta\varphi_E^-}| \end{cases} \quad \text{(A3)}$$

and

$$\delta\varphi_{j_e,j_m} = \varphi_{j_e} - \varphi_{j_m} = \mathrm{Arg}(-|E_z^+|e^{i\delta\varphi_E^+} - |E_z^-|e^{i\delta\varphi_E^-}) - \mathrm{Arg}(-|E_z^+|e^{i\delta\varphi_E^+} + |E_z^-|e^{i\delta\varphi_E^-}). \quad \text{(A4)}$$

The quantities $|E_z^+|$, $|E_z^-|$, $\delta\varphi_E^+$, and $\delta\varphi_E^-$ are derived from fitting with the numerically calculated fields and then plugged into Eqs. (A3) and (A4). In Fig. 17, a lasing snapshot is shown, overlapped with fitted outgoing sine waves. The snapshot shows a cross-section along the y axis [see Fig. 1(d) for orientation], where the peak of the dark mode can be identified around $y = 0$. For this particular example, the outgoing waves to which the dark mode couples exhibit preferential directionality towards $y < 0$.

Conversion of pump rate to material gain. Because the gain material is homogeneously embedded in the dielectric host medium of relative permittivity $\varepsilon_{r,\mathrm{host}}$, the polarization density P_a induced by the gain material adds to the host material polarization density P_{host} to give an overall displacement field D:

$$D = \varepsilon_0 E + P_{\mathrm{host}} + P_a = \varepsilon_0 \overbrace{\left(\underbrace{1+\chi_{\mathrm{host}}}_{\varepsilon_{r,\mathrm{host}}} + \underbrace{\frac{1}{\varepsilon_0}\frac{P}{E}}_{\chi_{\mathrm{gain}}}\right)}^{\varepsilon_{r,\mathrm{gain}}} E, \quad \text{(A5)}$$

where χ_{host} and χ_{gain} are the host and gain material susceptibilities, respectively, and $\varepsilon_{r,\mathrm{gain}}$ the total permittivity. χ_{gain} can be calculated from Eq. (A2) in steady state, so that

$$\varepsilon_{r,\mathrm{gain}} = \varepsilon_{r,\mathrm{host}} + \chi_{\mathrm{gain}} = \varepsilon_{r,\mathrm{host}} + \frac{1}{\varepsilon_0}\frac{P}{E} = \varepsilon_{r,\mathrm{host}} - \frac{1}{\varepsilon_0}\frac{\sigma_a(N_2-N_1)}{\omega_a^2 - \omega^2 + i\omega\Gamma_a}. \quad \text{(A6)}$$

What is unknown is the population difference $\Delta N = N_2 - N_1$, which is a function of the pump rate R_p. In order to calculate ΔN, we need to consider the equation system (A1) in the absence of any signal, in the limit of $t \to \infty$, where $d/dt \to 0$. This is because, although populations change once lasing has initiated, we only need to know the populations before the onset of lasing (these will provide the necessary gain for lasing to happen). Solution of Eq. (A1) yields

$$N_2 - N_1 = \frac{\tau_{30}(\tau_{21}-\tau_{10})R_p}{\tau_{32} + \tau_{30}[1 + R_p(\tau_{10}+\tau_{21}+\tau_{32})]}N_{\mathrm{total}}. \quad \text{(A7)}$$

Hence the gain coefficient is given by

$$\gamma = \frac{4\pi}{\lambda}\mathrm{Im}(\sqrt{\varepsilon_{r,\mathrm{gain}}}) = \frac{4\pi}{\lambda}\mathrm{Im}\left[\sqrt{\varepsilon_{r,\mathrm{host}} - \frac{1}{\varepsilon_0}\frac{\sigma_a(N_2-N_1)}{\omega_a^2 - \omega^2 + i\omega\Gamma_a}}\right]$$

or

$$\gamma = \frac{4\pi}{\lambda}\mathrm{Im}\left[\sqrt{\varepsilon_{r,\mathrm{host}} - \frac{1}{\varepsilon_0}\frac{\sigma_a}{\omega_a^2 - \omega^2 + i\omega\Gamma_a}\frac{\tau_{30}(\tau_{21}-\tau_{10})R_p}{\tau_{32} + \tau_{30}[1 + R_p(\tau_{10}+\tau_{21}+\tau_{32})]}N_{\mathrm{total}}}\right], \quad \text{(A8)}$$

which, assuming operation at the gain emission frequency $\omega \cong \omega_a$, is simplified as

$$\gamma = \frac{4\pi}{\lambda}\mathrm{Im}\left[\sqrt{\varepsilon_{r,\mathrm{host}} + i\frac{\sigma_a}{\varepsilon_0\omega_a\Gamma_a}\frac{\tau_{30}(\tau_{21}-\tau_{10})R_p}{\tau_{32} + \tau_{30}[1 + R_p(\tau_{10}+\tau_{21}+\tau_{32})]}N_{\mathrm{total}}}\right]. \quad \text{(A9)}$$

Relation of absorption cross-section to material permittivity. The absorption cross-section and the material permittivity are connected through the absorption coefficient, which for each case is given by $\alpha = \sigma_A(N_3 - N_0) \cong -\sigma_A N_0$ and

$\alpha = \frac{4\pi}{\lambda}\mathrm{Im}(\sqrt{\varepsilon_{r,\mathrm{gain}}})$. If we denote $\varepsilon_{r,\mathrm{gain}} = \varepsilon' + i\varepsilon''$ with $\varepsilon', \varepsilon'' \in \mathbb{R}$, then $\mathrm{Im}(\sqrt{\varepsilon_{r,\mathrm{gain}}}) = -\sqrt{\frac{\sqrt{\varepsilon'^2+\varepsilon''^2}-\varepsilon'}{2}}$ and we may write

$$\frac{4\pi}{\lambda}\sqrt{\frac{\sqrt{\varepsilon'^2+\varepsilon''^2}-\varepsilon'}{2}} = \sigma_A N_0 \quad \text{or} \quad \varepsilon'' = \sqrt{\left(2\left(\frac{\lambda}{4\pi}\sigma_A N_0\right)^2 + \varepsilon'\right)^2 - \varepsilon'^2}. \tag{A10}$$

Using Eq. (A10) with the columns of Table I for $\sigma_A, N = N_0$ and $\varepsilon' = n_{\mathrm{host}}^2$, we find ε'' for each gain material.

The double current sheet model. Let us assume two infinite electromagnetic sheets carrying surface currents J_1 and J_2. The sheets are separated by a distance d and divide space into three homogeneous regions, characterized by permittivities $\varepsilon_{r,1}$, $\varepsilon_{r,2}$, and $\varepsilon_{r,3}$, corresponding to regions 1, 2, and 3, respectively, as shown in Fig. 9. Application of the boundary conditions on each interface yields the fields in all three regions. The electric field in regions 1 and 3 is given by

$$E_z^{(-)} = \left(\left(\frac{C_b}{C_d} + r_{13}\frac{C_c}{C_d}\right)J_1 + \frac{C_a}{C_d}J_2\right)e^{i(\omega t + k_1 y)}, \quad y < 0 \tag{A11a}$$

$$E_z^{(+)} = \left(\frac{C_a}{C_d}J_1 + \left(\frac{C_b}{C_d} + r_{31}\frac{C_c}{C_d}\right)J_2\right)e^{i(\omega t - k_3 y)}, \quad y > d \tag{A11b}$$

where $k_i = \sqrt{\varepsilon_{r,i}}\frac{\omega}{c}$ is the wave number in region i and the parameters C_a, C_b, C_c, and C_d are given by

$$C_a = 2(\eta_1 + \eta_3)\mathrm{e}^{-ik_2 d}(r_{12} + r_{32}), \tag{A12a}$$

$$C_b = (\eta_1 + \eta_3)((\mathrm{e}^{-ik_2 d})^2(r_{12} + r_{32} - 1) + (r_{12} + r_{32} + 1)), \tag{A12b}$$

$$C_c = (\eta_1 + \eta_3)(1 - (\mathrm{e}^{-ik_2 d})^2), \tag{A12c}$$

$$C_d = (\mathrm{e}^{-ik_2 d})^2(r_{21} - 1)(r_{23} - 1)(r_{12} + r_{32})^2 - (r_{12} + 1)(r_{31} + 1)(r_{12} + r_{32})(r_{23} + 1). \tag{A12d}$$

With η_i denoting the wave impedance in region i, the wave impedance ratios r_{ij} are defined as

$$r_{ij} \triangleq \frac{\eta_i}{\eta_j} = \sqrt{\frac{\mu}{\varepsilon_{r,i}}}\Big/\sqrt{\frac{\mu}{\varepsilon_{r,j}}} = \sqrt{\frac{\varepsilon_{r,j}}{\varepsilon_{r,i}}}. \tag{A13a}$$

In terms of the symmetric J_S and antisymmetric J_A currents $\left.\begin{matrix} J_S = \frac{J_1+J_2}{2} \\ J_A = \frac{J_1-J_2}{2} \end{matrix}\right\} \Leftrightarrow \left\{\begin{matrix} J_1 = J_S + J_A \\ J_2 = J_S - J_A \end{matrix}\right.$, the outgoing waves are written as

$$E_z^{(-)} = \left(\left(\frac{C_a + C_b}{C_d} + r_{13}\frac{C_c}{C_d}\right)J_S - \left(\frac{C_a - C_b}{C_d} - r_{13}\frac{C_c}{C_d}\right)J_A\right)e^{i(\omega t + k_1 y)}, \quad y < 0 \tag{A14a}$$

$$E_z^{(+)} = \left(\left(\frac{C_a + C_b}{C_d} + r_{31}\frac{C_c}{C_d}\right)J_S + \left(\frac{C_a - C_b}{C_d} - r_{31}\frac{C_c}{C_d}\right)J_A\right)e^{i(\omega t - k_3 y)}, \quad y > d. \tag{A14b}$$

In our case: $\eta_1 = \eta_3 \triangleq \eta$ and hence $r_{13} = r_{31} = 1$ and $k_1 = k_3 \triangleq k$ and the fields are written in compact form as

$$E_z^{(\pm)} = \left(\left(\frac{C_a + C_b + C_c}{C_d}\right)J_S \pm \left(\frac{C_a - C_b - C_c}{C_d}\right)J_A\right)e^{i(\omega t \mp k y)}. \tag{A15}$$

Because $\varepsilon_{r,1} = \varepsilon_{r,3} \triangleq \varepsilon_{\mathrm{out}}$, the wave impedance ratios become $r_{32} = r_{12} = \sqrt{\frac{\varepsilon_{r,2}}{\varepsilon_{\mathrm{out}}}} \triangleq r$ and $r_{23} = r_{21} = \sqrt{\frac{\varepsilon_{\mathrm{out}}}{\varepsilon_{r,2}}} = \frac{1}{r}$. The coefficients C_a, C_b, C_c and C_d simplify as:

$$C_a = 8\eta\mathrm{e}^{-ik_2 d}r, \tag{A16a}$$

$$C_b = 2\eta((\mathrm{e}^{-ik_2 d})^2(2r - 1) + (2r + 1)), \tag{A16b}$$

$$C_c = 2\eta(1 - (\mathrm{e}^{-ik_2 d})^2), \tag{A16c}$$

$$C_d = 4((\mathrm{e}^{-ik_2 d})^2(1 - r)^2 - (1 + r)^2), \tag{A16d}$$

and the fields are written as

$$E_z^{(\pm)} = \left(\eta J_S\frac{2r\mathrm{e}^{-ik_2 d} + (\mathrm{e}^{-ik_2 d})^2(r - 1) + (r + 1)}{(\mathrm{e}^{-ik_2 d})^2(1 - r)^2 - (1 + r)^2} \pm \eta J_A\frac{2r\mathrm{e}^{-ik_2 d} - (\mathrm{e}^{-ik_2 d})^2(r - 1) - (r + 1)}{(\mathrm{e}^{-ik_2 d})^2(1 - r)^2 - (1 + r)^2}\right)e^{i(\omega t \mp k y)}. \tag{A17}$$

Comparing this result with Eq. (3a),

$$\frac{1}{2}\eta j_e = \left(\eta \frac{2re^{-ik_2d}(e^{-ik_2d})^2(r-1)+(r+1)}{-(e^{-ik_2d})^2(r-1)^2+(r+1)^2}\right) J_S, \tag{A18a}$$

and

$$\frac{1}{2} j_m = \left(\eta \frac{2re^{-ik_2d}-(e^{-ik_2d})^2(r-1)-(r+1)}{-(e^{-ik_2d})^2(r-1)^2+(r+1)^2}\right) J_A. \tag{A18b}$$

What is of importance to our study is not the absolute quantities j_e and j_m, but their relative amplitude and phase and hence we may use Eqs. (A18a) and (A18b) to write their ratio as

$$\frac{\eta j_e}{j_m} = \frac{2re^{-ik_2d}+(e^{-ik_2d})^2(r-1)+(r+1)}{2re^{-ik_2d}-(e^{-ik_2d})^2(r-1)-(r+1)} \frac{J_S}{J_A}. \tag{A19}$$

Separating the big fraction into real and imaginary part, we obtain

$$\frac{\eta j_e}{j_m} = \left(\frac{2(r^2-1)\cos\left(\frac{k_2d}{2}\right)^2}{(1-r^2)\cos(k_2D)+r^2+1} + i\cot\left(\frac{k_2d}{2}\right)\frac{2r}{\left(1-r^2\right)\cos(k_2d)+r^2+1}\right)\frac{J_S}{J_A}. \tag{A20}$$

If we write the complex current quantities as $j_e = |j_e|e^{i\varphi_{j_e}}$, $j_m = |j_m|e^{i\varphi_{j_m}}$, $J_S = |J_S|e^{i\varphi_{J_S}}$, and $J_A = |J_A|e^{i\varphi_{J_A}}$, we reach the result

$$\delta\varphi_{j_e,j_m} = \overbrace{\arctan\left(\frac{2r}{\left(r^2-1\right)\sin(k_2d)}\right)}^{\delta\varphi_{\text{slab}}} + \delta\varphi_{J_S,J_A}, \tag{A21}$$

where $\delta\varphi_{j_e,j_m} = \varphi_{j_e} - \varphi_{j_m}$ and $\delta\varphi_{J_S,J_A} = \delta\varphi_{J_S} - \delta\varphi_{J_A}$.

[1] K. Iga, Surface-emitting laser—its birth and generation of new optoelectronics field, IEEE J. Sel. Top. Quant. Electron. **6**, 1201 (2000).

[2] O. Painter, R. K. Lee, A. Scherer, A. Yariv, J. D. O'Brien, P. D. Dapkus, and I. Kim, Two-dimensional photonic band-gap defect mode laser, Science **284**, 1819 (1999).

[3] A. Tandaechanurat, S. Ishida, D. Guimard, M. Nomura, S. Iwamoto, and Y. Arakawa, Lasing oscillation in a three-dimensional photonic crystal nanocavity with a complete bandgap, Nat. Photonics **5**, 91 (2011).

[4] A. Yariv and P. Yeh, *Optical Electronics in Modern Communications* (Oxford University Press, New York, 2007).

[5] S. L. McCall, A. F. J. Levi, R. E. Slusher, S. J. Pearton, and R. A. Logan, Whispering-gallery mode microdisk lasers, Appl. Phys. Lett. **60**, 289 (1992).

[6] J. P. Zhang, D. Y. Chu, S. L. Wu, S. T. Ho, W. G. Bi, C. W. Tu, and R. C. Tiberio, Photonic-Wire Laser, Phys. Rev. Lett. **75**, 2678 (1995).

[7] D. J. Bergman and M. I. Stockman, Surface Plasmon Amplification by Stimulated Emission of Radiation: Quantum Generation of Coherent Surface Plasmons in Nanosystems, Phys. Rev. Lett. **90**, 027402 (2003).

[8] N. I. Zheludev, S. L. Prosvirnin, N. Papasimakis, and V. A. Fedotov, Lasing spaser, Nat. Photonics **2**, 351 (2008).

[9] R. F. Oulton, V. J. Sorger, T. Zentgraf, R.-M. Ma, C. Gladden, L. Dai, G. Bartal, and X. Zhang, Plasmon lasers at deep subwavelength scale, Nature (London) **461**, 629 (2009).

[10] M. I. Stockman, Spasers explained, Nat. Photonics **2**, 327 (2008).

[11] M. A. Noginov, G. Zhu, A. M. Belgrave, R. Bakker, V. M. Shalaev, E. E. Narimanov, S. Stout, E. Herz, T. Suteewong, and U. Wiesner, Demonstration of a spaser-based nanolaser, Nature (London) **460**, 1110 (2009).

[12] M. I. Stockman, The spaser as a nanoscale quantum generator and ultrafast amplifier, J. Opt. **12**, 024004 (2010).

[13] P. Berini and I. De Leon, Surface plasmon-polariton amplifiers and lasers, Nat. Photonics **6**, 16 (2012).

[14] S. Wuestner, A. Pusch, K. L. Tsakmakidis, J. M. Hamm, and O. Hess, Overcoming Losses with Gain in a Negative Refractive Index Metamaterial, Phys. Rev. Lett. **105**, 127401 (2010).

[15] O. Hess, J. B. Pendry, S. A. Maier, R. F. Oulton, J. M. Hamm, and K. L. Tsakmakidis, Active nanoplasmonic metamaterials, Nat. Mater. **11**, 573 (2012).

[16] X. L. Zhong and Z. Y. Li, All-analytical semiclassical theory of spaser performance in a plasmonic nanocavity, Phys. Rev. B **88**, 085101 (2013).

[17] J. B. Khurgin, and G. Sun, Comparative analysis of spasers, vertical-cavity surface-emitting lasers and surface-plasmon-emitting diodes, Nat. Photonics **8**, 468 (2014).

[18] S. Droulias, A. Jain, P. Tassin, T. Koschny, and C. M. Soukoulis, Novel Lasers Based on Resonant Dark States, Phys. Rev. Lett. **118**, 073901 (2017).

[19] A. Jain, P. Tassin, T. Koschny, and C. M. Soukoulis, Large Quality Factor in Sheet Metamaterials Made from Dark Dielectric Meta-Atoms, Phys. Rev. Lett. **112**, 117403 (2014).

[20] N. Yu, and F. Capasso, Flat optics with designer metasurfaces, Nat. Mater. **13**, 139 (2014).

[21] S. Jahani and Z. Jacob, All-dielectric metamaterials, Nat. Nanotechnol. **11**, 23 (2016).
[22] A. I. Kuznetsov, A. E. Miroshnichenko, M. L. Brongersma, Y. S. Kivshar, and B. Luk'yanchuk, Optically resonant dielectric nanostructures, Science **354**, aag2472 (2016).
[23] S. Wuestner, A. Pusch, K. L. Tsakmakidis, J. M. Hamm, and O. Hess, Gain and plasmon dynamics in active negative-index metamaterials, Philos. Trans. R. Soc. A **369**, 3525 (2011).
[24] J. M. Hamm, S. Wuestner, K. L. Tsakmakidis, and O. Hess, Theory of Light Amplification in Active Fishnet Metamaterials, Phys. Rev. Lett. **107**, 167405 (2011).
[25] K. L. Tsakmakidis and O. Hess, Extreme control of light in metamaterials: Complete and loss-free stopping of light, Physica B **407**, 4066 (2012).
[26] O. Hess and K. L. Tsakmakidis, Metamaterials with quantum gain, Science **339**, 654 (2013).
[27] S. Wuestner, J. M. Hamm, A. Pusch, F. Renn, K. L. Tsakmakidis, and O. Hess, Control and dynamic competition of bright and dark lasing states in active nanoplasmonic metamaterials, Phys. Rev. B **85**, 201406(R) (2012).
[28] N. Meinzer, M. Ruther, S. Linden, C. M. Soukoulis, G. Khitrova, J. Hendrickson, J. D. Olitzky, H. M. Gibbs, and M. Wegener, Arrays of Ag split-ring resonators coupled to InGaAs single-quantum-well gain, Opt. Express **18**, 24140 (2010).
[29] N. Meinzer, M. König, M. Ruther, S. Linden, G. Khitrova, H. M. Gibbs, K. Busch, and M. Wegener, Distance-dependence of the coupling between split-ring resonators and single-quantum-well gain, Appl. Phys. Lett. **99**, 111104 (2011).
[30] P. B. Johnson and R. W. Christy, Optical constants of the noble metals, Phys. Rev. B **6**, 4370 (1972).
[31] N.-H. Shen, T. Koschny, M. Kafesaki, and C. M. Soukoulis, Optical metamaterials with different metals, Phys. Rev. B **85**, 075120 (2012).
[32] O. Svelto, *Principles of Lasers*, 4th ed. (Springer, New York, USA, 1998).
[33] W. T. Silfvast, *Laser fundamentals*, 2nd ed. (Cambridge University Press, USA, 2004).
[34] W. L. Barnes, R. I. Laming, E. J. Tarbox, and P. R. Morkel, Absorption and emission cross section of Er^3 doped silica fibers, IEEE J. Quantum Electron. **27**, 1004 (1991).
[35] J. N. Sandoe, P. H. Sarkies, and S. Parke, Variation of Er^3 cross section for stimulated emission with glass composition, J. Phys. D: Appl. Phys. **5**, 1788 (1972).
[36] P. Sperber, W. Spangler, B. Meier, and A. Penzkofer, Experimental and theoretical investigation of tunable picosecond pulse generation in longitudinally pumped dye laser generators and amplifiers, Opt. and Quantum Electr. **20**, 395 (1988).
[37] A. Penzkofer and W. Leupacher, Fluorescence behaviour of highly concentrated Rhodamine 6G solutions, J. Lumin. **37**, 61 (1987).
[38] O. G. Peterson, J. P. Webb, W. C. McColgin, and J. H. Eberly, Organic dye laser threshold, J. Appl. Phys. **42**, 1917 (1971).
[39] T. Susdorf, D. Del Agua, A. Tyagi, A. Penzkofer, O. García, R. Sastre, A. Costela, and I. García-Moreno, Photophysical characterization of pyrromethene 597 laser dye in silicon-containing organic matrices, Appl. Phys. B **86**, 537 (2007).
[40] J. H. Yan, C. G. Wang, H. Zhang, and C. Cheng, Evaluation of emission cross section of CdSe quantum dots for laser applications, Laser Phys. Lett. **9**, 529 (2012).
[41] C. Cheng, Y. Xu, and X. Cheng, Near-infrared absorption–emission cross-sections of PbSe quantum dots doped in UV gel, Opt. Commun. **347**, 108 (2015).
[42] S. W. Corzine and L. A. Coldren, Theoretical gain in compressive and tensile strained InGaAs/InGaAsP quantum wells, Appl. Phys. Lett. **59**, 588 (1991).
[43] H. Carrère, X. Marie, L. Lombez, and T. Amand, Optical gain of InGaAsN/InP quantum wells for laser applications, Appl. Phys. Lett. **89**, 181115 (2006).
[44] A. E. Siegman, *Lasers* (University Science, Sausalito, CA, 1986).
[45] P. Tassin, T. Koschny, and C. M. Soukoulis, Effective material parameter retrieval for thin sheets: Theory and application to graphene, thin silver films, and single-layer metamaterials, Physica B **407**, 4062 (2012).
[46] S. Xiao, V. P. Drachev, A. V. Kildishev, X. Ni, U. K. Chettiar, H.-K. Yuan, and V. M. Shalaev, Loss-free and active optical negative-index metamaterials, Nature (London) **466**, 735 (2010).
[47] S. Riechel, C. Kallinger, U. Lemmer, J. Feldmann, A. Gombert, V. Wittwer, and U. Scherf, A nearly diffraction limited surface emitting conjugated polymer laser utilizing a two-dimensional photonic band structure, Appl. Phys. Lett. **77**, 2310 (2000).
[48] E. Plum, V. A. Fedotov, P. Kuo, D. P. Tsai, and N. I. Zheludev, Towards the lasing spaser: Controlling metamaterial optical response with semiconductor quantum dots, Opt. Express **17**, 8548 (2009).
[49] K. Tanaka, E. Plum, J. Y. Ou, T. Uchino, and N. I. Zheludev, Multifold Enhancement of Quantum Dot Luminescence in Plasmonic Metamaterials, Phys. Rev. Lett. **105**, 227403 (2010).
[50] A. Fang, T. Koschny, and C. M. Soukoulis, Lasing in metamaterial nanostructures, J. Opt. **12**, 024013 (2010).
[51] A. Fang, T. Koschny, and C. M. Soukoulis, Self-consistent calculations of loss-compensated fishnet metamaterials, Phys. Rev. B **82**, 121102(R) (2010).
[52] A. Fang, Z. Huang, T. Koschny, and C. M. Soukoulis, Overcoming the losses of a split ring resonator array with gain, Opt. Express **19**, 12688 (2011).
[53] Z. Huang, T. Koschny, and C. M. Soukoulis, Theory of Pump-Probe Experiments of Metallic Metamaterials Coupled to a Gain Medium, Phys. Rev. Lett. **108**, 187402 (2012).
[54] Z. Huang, S. Droulias, T. Koschny, and C. M. Soukoulis, Mechanism of the metallic metamaterials coupled to the gain material, Opt. Express **22**, 28596 (2014).
[55] A. Taflove, *Computational Electrodynamics: The Finite Difference Time Domain Method* (Artech House, London, 1995).